

Using near-flat-band electrons for read-out of molecular spin qubit entangled states

Christian Bunker,[†] Silas Hoffman,[‡] Shuanglong Liu,[¶] Xiao-Guang Zhang,[†] and
Hai-Ping Cheng^{*,¶}

[†]*Department of Physics, Center for Molecular Magnetic Quantum Materials, and Quantum Theory Project, University of Florida, Gainesville, Florida 32611*

[‡]*Laboratory for Physical Sciences, College Park, Maryland 20740*

[¶]*Department of Physics, Northeastern University, Boston, Massachusetts 02115*

E-mail: ha.cheng@northeastern.edu

Abstract

While molecular spin qubits (MSQs) are a promising platform for quantum computing, read-out has been largely limited to electron paramagnetic resonance which is often slow and requires a global system drive. Moreover, because one prerequisite for the Elzerman and Pauli spin blockade readout mechanisms typical of semiconductor spin qubits is tunneling of electrons between sites, these read-out modalities are unavailable in MSQs. Here, we theoretically demonstrate electrical read-out of entangled MSQs *via* driven many-electron spin unpolarized currents. In particular, using a time-dependent density matrix renormalization group approach we simulate a maximally entangled MSQ pair between two electronic leads. Driving itinerant electrons between the two leads, we find that the conductance is greater when the MSQs are in the entangled singlet state as compared to the entangled triplet state. This contrast in conductance is enhanced when the electronic density of states at the Fermi energy is large and for

narrow bandwidth. Our results are readily applicable to molecules supramolecularly functionalizing semiconductors with relatively flat bands such as single-wall carbon nanotubes under a magnetic field.

Keywords

Quantum computing, molecular spin qubits, qubit read-out, singlet-triplet qubits, magnetic molecules

Introduction

Itinerant electrons coupled to quantum information^{1,2} stored in the spin degree of freedom of a localized particle such as a semiconductor spin qubit^{3,4} or a molecular spin qubit (MSQ)⁵⁻⁷ offer a promising avenue towards functional quantum information science devices.⁸ Electrons are particularly well suited to generating and probing entanglement between pairs of spin qubits,⁹⁻¹⁴ a key task for quantum information science. For example, maximally entangling two qubits using an electron as a measurement ancilla has been proposed^{9,10} and demonstrated.¹⁵ Further, using itinerant electrons to electrically probe and read-out qubit states enables compact, scalable qubits^{8,16,17} based largely on architectures that have already been optimized by the semiconductor industry.¹⁸⁻²⁰

For semiconductor spin qubits, spin-to-charge conversion^{4,21} is a trusted electrical read-out protocol requiring tunneling of the qubit electrons. Unlike in semiconductors, MSQs lack convenient tunneling barrier control, so facilitating tunneling is difficult.¹⁷ Alternatively, a measurement of the *conductance* past or through the MSQs avoids tunneling.¹⁷ Conductance measurements have been experimentally demonstrated to read-out the quantum state of *single* spins,¹⁷ but extending conductance-based read-out to multi-spin molecular qubit encodings such as singlet-triplet qubits remains to be demonstrated.

Singlet-triplet (ST_0) qubits⁴ embed one logical qubit within the maximally entangled

two-spin states

$$|\psi_{\text{qubit}}\rangle = (|\uparrow_1\downarrow_2\rangle + e^{i\phi_{\text{ent}}}|\downarrow_1\uparrow_2\rangle)/\sqrt{2} \quad (1)$$

where $|\psi_{\text{qubit}}\rangle = |S\rangle$ ($\phi_{\text{ent}} = \pi$) and $|\psi_{\text{qubit}}\rangle = |T_0\rangle$ ($\phi_{\text{ent}} = 0$) define the logical states. This qubit encoding benefits from fast state preparation and read-out as well as minimal decoherence under global magnetic field fluctuations.²² Electrical read-out of semiconductor ST_0 qubits relies on Pauli spin blockade.²¹⁻²⁴ However, since Pauli spin blockade requires the tunneling control typically lacking in MSQ architectures, the ability to measure conductance for electrical read-out of molecular ST_0 qubits in addition to single spins remains a desirable objective.

MSQ read-out *via* correlation between the conductance and $|\psi_{\text{qubit}}\rangle$ would require interaction between entangled MSQ states and itinerant electrons, such as those arising in supramolecular devices²⁵⁻²⁸ comprising semiconducting nanowires, for example single-wall carbon nanotubes or graphene nanoribbons, functionalized by MSQs. These systems feature MSQ spins exerting effective torque on the itinerant electron spins known as *sd* exchange,²⁵ similar^{29,30} to the Kondo interaction^{31,32} between itinerant electrons and magnetic impurities in metals, and measured in the 0.1-1 meV range in supramolecular devices.^{25,28} We describe specific chemical realizations of *sd* exchange for MSQs deposited on semiconductor nanowires in the discussion. Ref. 14 was the first to show that *sd* exchange links the conductance to the ST_0 qubit states (1), showing that for $\phi_{\text{ent}} = \pi$, constructive interference makes the conductance essentially perfect, while $\phi_{\text{ent}} = 0$ impedes the conductance.^{14,33} Ref. 14 further demonstrated that this conductance disparity grew with increasing density of states in the semiconductor nanowire. The conductance dependence on $|\psi_{\text{qubit}}\rangle$, modulated by ϕ_{ent} ,^{14,33,34} is a quantum analogue of a classical spin valve in which conductance depends on the relative polarization between two ferromagnetic leads.³⁵⁻³⁹ Consequently, we refer to the conductance dependence discovered in Ref. 14 as the *quantum spin-valve effect*. Just

as the classical spin valve effect can be leveraged for read-out of classical bits, the quantum spin-valve effect enables read-out of ST_0 qubits.

Despite the exciting applications of quantum spin valves to reading-out molecular ST_0 qubits, understanding of these systems remains immature. Supramolecular devices^{25–28} have experimentally demonstrated classical spin valve physics but have not yet shown conductance measurements sensitive to inherently quantum states such as the entangled $|S\rangle$ and $|T_0\rangle$ states. On the theory side, Ref. 14 used a single-particle wavefunction matching method to simulate the conductance of a single electron only, which cannot speak to the viability of the quantum spin valve effect and its application to read-out in a realistic many-electron semiconductor nanowire. To build on this work, we use many-body transport methods to simulate entangled MSQs interacting with a *many-electron* current, thereby exploring quantum spin valve physics in the more-realistic regime beyond single-electron scattering. The time-dependent density matrix renormalization group (td-DMRG) method^{40–42} is a well-established approach to the many-body transport problem^{43–47} capable of simulating a many-electron scenario. td-DMRG is a family of algorithms for representing, variationally minimizing, and time-evolving correlated many-body quantum states. To study many-body transport, we apply the td-DMRG algorithm^{40,41,43} to time evolve the initial many-body state under a quenched Hamiltonian using the time-dependent variational principle,⁴⁸ performing this calculation with the BLOCK2 code.⁴⁹ In these calculations, we find that an efficient many-electron quantum spin valve is possible.

To further Ref. 14’s observation that the quantum-spin valve effect hinges on enhancing the density of states at the Fermi energy, our model Hamiltonian explicitly allows tunable band structure to probe how the underlying electronic properties of the nanowire impact the physics of the quantum spin valve. Specifically, instead of a tight-binding model with fixed bandwidth as in Ref. 14, we use the Rice-Mele model to control the band structure, *e.g.* the flatness of the band, *via* the tight-binding parameters. The Rice-Mele model^{50,51} is one-dimensional tight-binding model with staggered hopping terms, originally formulated to

describe π -conjugated polymers.^{52–54} The tunable staggered hopping terms enable Rice-Mele to capture the flat-band regime and tune other relevant electronic properties of the bands such as the bandgap or density of states. Drawing on π -conjugated^{26,55} flat-band materials,⁵⁶ such as twisted bilayer graphene (TBG)^{57,58} and its nanoribbon form,⁵⁹ doped graphene,⁶⁰ rhombohedral multilayer graphene,^{61,62} and single wall carbon nanotubes (SWCNTs)^{63–65} as exemplary realizations (Fig. 1) of π -conjugated nanowires with enhanced density of states, our results show that the quantum spin valve efficiency is greatly increased in the flat-band limit.

Results and discussion

Model System

The model Hamiltonian for our system (Fig. 2) should couple the MSQs to itinerant electrons in the semiconducting nanowire and be flexible enough to capture different band structure regimes in the nanowire. We write down a model Hamiltonian with sd exchange and tunable band structure arising from Rice-Mele tight-binding terms:

$$\begin{aligned}
\hat{H}(t) = & v \sum_{j=0}^{N_{\text{total}}-1} \sum_{\sigma} (c_{jA\sigma}^{\dagger} c_{jB\sigma} + c_{jB\sigma}^{\dagger} c_{jA\sigma}) \\
& + w \sum_{j=0}^{N_{\text{total}}-2} \sum_{\sigma} (c_{jB\sigma}^{\dagger} c_{j+1,A\sigma} + c_{j+1,A\sigma}^{\dagger} c_{jB\sigma}) \\
& - \frac{J_{sd}}{\hbar} \sum_{j=N_L}^{N_L+N_{SR}-1} \sum_{\sigma\sigma'\nu} \left(S_{d=2j-2N_L}^{\nu} c_{jA\sigma}^{\dagger} \sigma_{\sigma\sigma'}^{\nu} c_{jA\sigma'} \right. \\
& \quad \left. + S_{d=2j+1-2N_L}^{\nu} c_{jB\sigma}^{\dagger} \sigma_{\sigma\sigma'}^{\nu} c_{jB\sigma'} \right) \\
& + \theta(-t) \hat{H}_0,
\end{aligned} \tag{2}$$

where $0 \leq j \leq N_{\text{total}} - 1$ discretizes the nanowire into a one-dimensional chain of tight-

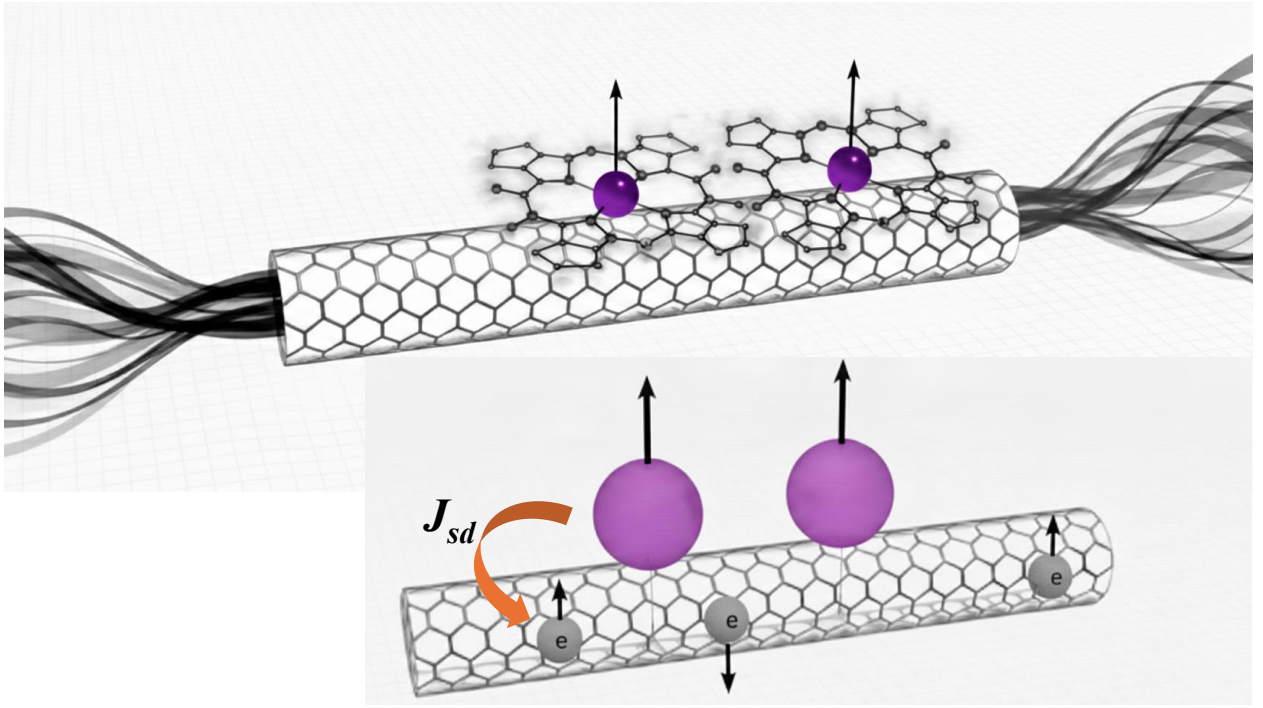


Figure 1: Top: Exemplary schematic of a supramolecular device where MSQs (purple) retain their magnetic properties as they functionalize a π -conjugated nanowire. Bottom: Our model describes itinerant electrons in the nanowire interacting with the spin degree of freedom of the MSQs only, *via* an exchange interaction of strength $J_{sd} \approx 1$ meV . Image created with Gemini.

binding unit cells of width a , and $\mu = A, B$ indexes the site degree of freedom within the cell. Here $c_{j\mu\sigma}^{(\dagger)}$ destroys (creates) an electron with spin $\sigma \in [\uparrow, \downarrow]$ on site μ of unit cell j , σ^ν are the Pauli matrices for $\nu = x, y, z$, and there are N_e total electrons. The hopping from A to B sites in the same unit cell is v , while the hopping from B to A sites in the next unit cell is w . The unit cells are partitioned into the left lead $0 \leq j \leq N_L - 1$, the scattering region $N_L \leq j \leq N_L + N_{SR} - 1$, and the right lead $N_L + N_{SR} \leq j \leq N_{\text{total}} - 1$. For each site in the scattering region exactly one MSQ couples to the electronic spin occupying the site *via* an exchange interaction J_{sd} . J_{sd} describes itinerant electrons traversing the nanowire such that their occupation of the MSQs is suppressed, and Coulomb interactions therein are treated as virtual processes. The MSQs are spin-1/2s with no spatial degrees of freedom, but are described by their generators of rotation in spin space $S_d^\nu = \frac{\hbar}{2}\sigma_d^\nu$ for the d^{th} MSQ. For the MSQ basis states we choose the eigenstates satisfying $S_d^z|\sigma_d\rangle = \pm\frac{\hbar}{2}|\sigma_d\rangle$ where $+(-)$ is for

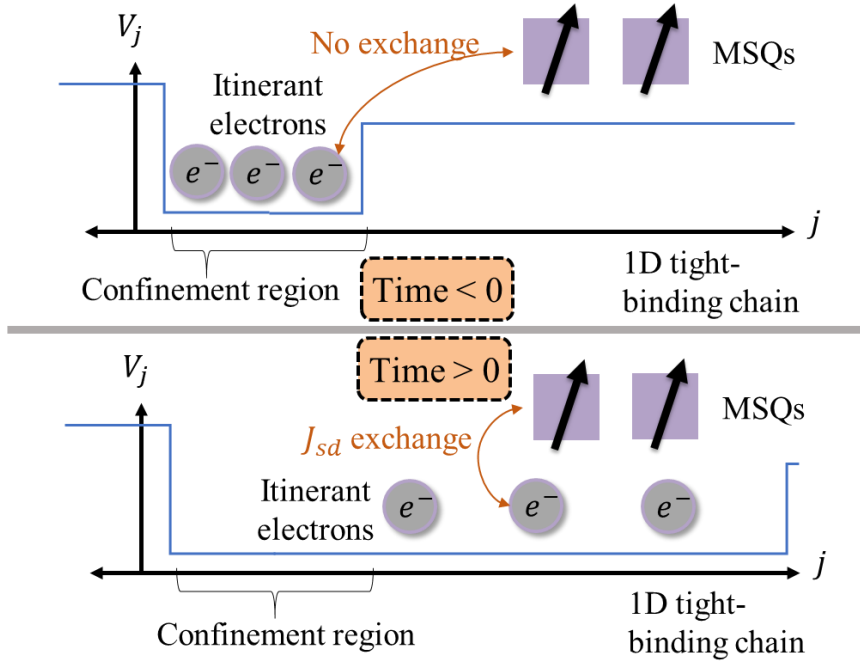


Figure 2: Model system: itinerant electrons live in a finite 1D nanowire. After a quantum quench at time zero, they spread out and interact with MSQs (purple) atop the nanowire. When the itinerant electrons are close to the MSQs, virtual hopping onto the MSQs yields sd exchange J_{sd} but no Coulomb interactions.

$\sigma = \uparrow (\downarrow)$.

The staggered Rice-Mele hopping terms v and w model the band structure with customizable bandgap and bandwidth set by w/v as discussed in the Supplementary Information. Setting $v = -1$ ensures the overall energy scale agrees with the material-specific bandwidth, while we vary w to tailor the band structure. While the Rice-Mele model is the tool we have chosen to modify the band structure of the semiconductor nanowire and probe its effect on the quantum spin valve, any experimental realization of a quantum spin valve need not be described by Rice-Mele.

In the last term in Eq. (2), $\theta(t)$ is the Heaviside function and \hat{H}_0 prepares the $t < 0$

system state, confining the electrons and entangling the MSQs according to

$$\hat{H}_0 = -V_{\text{conf}} \sum_{j=0}^{N_L-1} \sum_{\mu} \sum_{\sigma} c_{j\mu\sigma}^{\dagger} c_{j\mu\sigma} \quad (3)$$

$$- \sum_{d=0}^{N_{SR}-1} \left(\frac{J_{\text{ent}} - iJ'_{\text{ent}}}{2\hbar^2} S_{2d}^+ S_{2d+1}^- + \frac{J_{\text{ent}} + iJ'_{\text{ent}}}{2\hbar^2} S_{2d}^- S_{2d+1}^+ \right)$$

where $S_d^{\pm} = S_d^x \pm iS_d^y$ and the $J_{\text{ent}}, J'_{\text{ent}}$ parameters determine $|\psi_{\text{qubit}}\rangle$ according to Eq. (22). The term $\theta(-t)\hat{H}_0$ equals zero after time zero, amounting to a *quantum quench* (for a review see Ref. 66) of the system under which the $t < 0$ state of the system [the ground state of $\hat{H}(t < 0)$] is not an eigenstate of $\hat{H}(t > 0)$ so the dynamics are nontrivial. As sketched in Fig. 2, removing the V_{conf} term causes the itinerant electrons' wavefunctions spread out, simulating the injection of a current pulse into the nanowire.⁴³ Until it encounters the MSQs, the profile of this current pulse is determined by the single-particle eigenstates of $\hat{H}(t < 0)$ occupied by the electrons, as discussed in the Supplementary Information . Using the Rice-Mele model for the electronic Hamiltonian allows us to explore different regimes (*e.g.* a flat band structure) for these eigenstates that we would otherwise be unable to investigate.

Results

Our finite system contains a left lead of $N_L = 15$ unit cells, a scattering region of $N_{SR} = 1$ unit cells containing two MSQs, and a right lead of $N_R = 15$ unit cells, with $N_e = 10$ electrons confined to the left lead at $t < 0$ by \hat{H}_0 . As stated in Model System the unit cell j has site $\mu = A$ on the left and $\mu = B$ on the right, so that the 62 sites $|j\mu\rangle$ spanning the system fall into a one-dimensional chain. The choice of 10 electrons, although far smaller than the current in many nanojunctions, has been experimentally achieved in STM experiments with picoampere currents applied for nanosecond pulses.⁶⁷ Our results track the dynamics of this system under Eq. (2) after the quantum quench removes \hat{H}_0 , paying special attention to the occupation $n_{j\mu} = \sum_{\sigma} \langle c_{j\mu\sigma}^{\dagger} c_{j\mu\sigma} \rangle$ of each site $|j\mu\rangle$ along the one-dimensional chain and mutual

information I between MSQs [Eq. (8)] as a function of time t , which is measured in units of $\hbar/|v|$.

The quantum quench of the system initiates transport wherein the site occupation spreads rightward out of the left lead. This can be immediately seen in our heatmap results displaying the site occupation $n_{j\mu}$ as a function of time (Fig. 3). We begin with the heatmap simulated when the MSQs are absent, making several remarks about the transport properties independent of the effects of $|\psi_{\text{qubit}}\rangle$. First, after a certain time the electrons are observed to reflect off the right boundary $j = N_{\text{total}} - 1$ of the finite system we are simulating. The onset time for this reflection t_{fin} demarcates when our finite-size simulations honestly depict the dynamics of an open system ($t < t_{\text{fin}}$)⁴³ from when our simulations no longer capture such dynamics ($t > t_{\text{fin}}$). In Fig. 3 finite-size effects can be seen at $t_{\text{fin}} = 60$. We present and discuss our definition of t_{fin} in Eq. (18). We emphasize here that the timescale t_{fin} is an important property of each transport simulation.

Second, to rigorously quantify the rightward transport for a given MSQ state, we measure

$$n_R(t, \phi_{\text{ent}}) = \sum_{j=N_L+N_{SR}}^{N_{\text{total}}-1} \sum_{\mu} \sum_{\sigma} \langle c_{j\mu\sigma}^{\dagger} c_{j\mu\sigma} \rangle, \quad (4)$$

the electron accumulation in the right lead at time t when the phase of $|\psi_{\text{qubit}}\rangle$ [Eq. (1)] is ϕ_{ent} . Our simulations are not accurate past $t = t_{\text{fin}}$ so we always report $n_R(t_{\text{fin}})$. We note that experimentally, $n_R(t_{\text{fin}})$ represents the integrated current through the junction over the window $[0, t_{\text{fin}}]$ and that an experimentalist could modulate the length of time the current is applied for to maximize the measured $n_R(t)$ signal.

To probe quantum spin valve physics, we compare heatmap results for transport past initially entangled MSQ states in the family $|\psi_{\text{qubit}}\rangle$ defined by ϕ_{ent} . One descriptor of the MSQs throughout the transport is their mutual information I , which starts at $I = \ln(2)$ indicating maximal entanglement and decays with electron-MSQ interactions. In Fig. 3 we see that both $|T_0\rangle$ and $|S\rangle$ lose the majority of their entanglement (see I in the lower plot of

each panel). We also observe that the electrons pass the $|S\rangle$ MSQs and accumulate in the right lead, indicating an ‘open’ quantum spin valve with good conductance. For the single-electron transport in Ref. 14 $|T_0\rangle$ becomes a corresponding ‘closed’ quantum spin valve where the electron reflects off the MSQs rather than accumulating in the right lead. We aim to replicate this disparity between $|S\rangle$ and $|T_0\rangle$ for many electrons, however, the results for the trivial Rice-Mele band $w = v = -1$ (Fig. 3) the $n_{j\mu}$ heatmaps appear similar for both states. To rigorously define the difference in transport across MSQ states, we introduce the quantum spin valve efficiency

$$\eta(t_{\text{fin}}) = \frac{n_R(t_{\text{fin}}, \phi_{\text{ent}} = \pi) - n_R(t_{\text{fin}}, \phi_{\text{ent}} = 0)}{n_R(t_{\text{fin}}, \phi_{\text{ent}} = \pi) + n_R(t_{\text{fin}}, \phi_{\text{ent}} = 0)}. \quad (5)$$

The efficiency quantifies how the conductance of the open state $|S\rangle$ differs from the closed state $|T_0\rangle$ analogously to the magnetoresistance of a classical spin valve.³⁹ For Fig. 3 we calculate a relatively poor $\eta = 0.18$ so this does not yet replicate an efficient many-electron quantum spin valve.

Having established that the results in Fig. 3 fail to realize a high-efficiency quantum spin valve, we look at how varying the electronic properties can strengthen the efficiency. At the level of our simulation, varying electronic properties means adjusting the Hamiltonian parameters, particularly w , in order to tailor the $t < 0$ many-body state of the system, $|\Psi(t < 0)\rangle$ given in Eq. (21)]. For the electronic degrees of freedom, $|\Psi(t < 0)\rangle$ comprises the single-particle eigenstates shown in Fig. 5 occupied by the itinerant electrons. These single-particle eigenstates physically determine the energy and momentum of the electrons during transport. In subsequent results, we change the Hamiltonian parameters, calculate $|\Psi(t < 0)\rangle$ and the physically observable electronic properties such as $\rho(E_F)$, and finally determine the changes in the quantum spin valve simulations, particularly η . Note that properties such as $\rho(E_F)$, arising from the Hamiltonian, are realistic as long as the Hamiltonian parameters are realistic¹.

¹Given that we apply Rice-Mele, a two-band model, to emulate the band structure of a real material, we

Density of States Enhancement

To strengthen the quantum spin-valve efficiency, we try customizing $\rho(E)$. For a single band model (blue curve in Fig. 5) $\rho(E)$ only changes as the energy approaches the band edge, so density of states enhancement would have to proceed through ensuring itinerant electron energies are near the band edge, a challenging task of experimental control. A simpler approach is flattening the bandwidth to enhance the density of states across all energy states, which we can do within the Rice-Mele model by detuning w in the regime $w < 0$, $|w| < |v|$. This should strengthen the quantum spin-valve efficiency, has the additional advantage of not relying on the precise number of electrons or their distribution in energy space.

Now taking $w = -0.40$ to flatten the bandwidth to $E_{\text{band}} = 0.40$, in Fig. 5 we observe that $\rho(E)$ is uniformly enhanced compared to values closer to $w = v$. Looking at the electron accumulation for $|S\rangle$ vs. $|T_0\rangle$ in Fig. (4), thanks to the $\rho(E)$ enhancement the conductance dependence on the MSQ state can be seen by eye and the quantum spin valve efficiency has been increased to $\eta = 0.40$. As with the $w = v$ simulation, I is perturbed from its initially maximally entangled value $I = \ln(2)$ during the transport, but now we see that $|S\rangle$ retains more entanglement meaning it is less coupled to the itinerant electrons.

Quantum Spin Valve

The increase in quantum spin valve efficiency from $\eta = 0.18$ when $w = -1.00$ in Fig. 3 to $\eta = 0.40$ when $w = -0.40$ in Fig. 4 serves as a proof of concept for how using the Rice-Mele hopping to engineer electronic properties impacts the quantum spin valve efficiency. In Fig 6 we show the full trend where enhancing the density of states at the Fermi energy $\rho(E_F)$ monotonically increases the efficiency of the quantum spin valve. We can also look at the mutual information: for an efficient quantum spin valve, $|S\rangle$ decouples more from the itinerant electrons and so should retain more entanglement between MSQs over the

ensure Hamiltonian parameters are reasonable by comparing features of our bands to real band structure. For example, setting $|v| = 5$ meV ensures that the bandwidth in our model when $w = 0.4v$ agrees with the bandwidth reported for magic-angle twisted bilayer graphene.⁶⁸

simulation. Within td-DMRG we can quantify the MSQ-MSQ entanglement with the mutual information I and we see that I also increases with $\rho(E_F)$. The inset illustrates how the Rice-Mele hopping w directly determines the bandwidth and $\rho(E_F)$.

Beyond the efficiency, we can also explore how $\rho(E_F)$ impacts the detailed dependence of the conductance on all the entangled states in the family (1). In Fig. 7, we sweep over the values of ϕ_{ent} defining the maximally entangled states between $|T_0\rangle$ ($\phi_{\text{ent}} = 0$) and $|S\rangle$ ($\phi_{\text{ent}} = \pi$). Remarkably, our quantum spin valve is not just a bimodal device but *continuously tunes* its conductance from lower to higher as we sweep ϕ_{ent} . Further, we see increasing $\rho(E_F)$ increases the gradient across this sweep just as it increases η .

Qubit Read-Out

For read-out of ST_0 qubits the full Hilbert space includes the maximally entangled states $|S\rangle$, $|T_0\rangle$ and the unentangled states $|T_+\rangle = |\uparrow_1\uparrow_2\rangle$, $|T_-\rangle = |\downarrow_1\downarrow_2\rangle$. A conventional Pauli spin blockade experiment²¹⁻²⁴ shows an electrical signal as a qubit charge tunnels for the $|S\rangle$ state but no such signal for the $|T_{\pm}\rangle$ or $|T_0\rangle$ states, distinguishing $|S\rangle$ from the triplet family of states. We now ask whether we can apply the quantum spin valve physics to make the same distinction for MSQs. This would allow a measurement of the nanowire conductance, which has already been applied to experimental read-out of spin states in molecules,^{17,69,70} to replace Pauli spin blockade in reading-out molecular ST_0 qubits. This replacement is desirable since MSQs lack the tunneling control characteristic of semiconductor spin qubits in gate-defined quantum dots,²³ a necessary condition to achieve the Pauli spin blockade tunneling signal¹⁷ ².

In Fig. 8, we illustrate the electron accumulation [Eq. (4)] results for $|S\rangle$ vs. the entire family of triplet states. Remarkably, we see that not only does the density of states enhancement separate the measured accumulation of $|S\rangle$ from $|T_0\rangle$ as we have seen with the quantum spin valve, it distinguishes all the triplet states from $|S\rangle$. A conductance measurement for

²In fact, the latest high-fidelity Pauli spin blockade schemes involve charge-latching²³ which requires even more electron tunneling control

the two MSQs deposited atop the nanowire thus stands as a suitable analogue of Pauli spin blockade that allows read-out of ST_0 qubits encoded in molecules. The electrical signal of high conductance (high electron accumulation) distinguishes $|S\rangle$ from $|T_{\pm}\rangle$ and $|T_0\rangle$. Of course, in any real experiment one wants to maximize the strength of this signal to increase the fidelity of assigning a measurement to a singlet or triplet state. Our results show that *the density of states enhancement serves as the physical knob for optimizing the read-out fidelity* through increasing the quantum spin valve efficiency. Although in this paper we used the Rice-Mele hopping to tune this knob, an experimenter is not limited to systems with staggered hopping but must simply be able to enhance $\rho(E_F)$.

Discussion

The supramolecular devices^{25–28} we model in this work consist of MSQs that retain their magnetic properties when noncovalently functionalizing^{26,71–75} π -conjugated nanowires. Our model assumes (i) a π -mediated sd exchange between the itinerant electrons of the π -conjugated nanowire and the MSQs and (ii) flat-band electronic dispersion in the nanowire. We now discuss whether the components of this model are manifest in the experimental literature.

For a chemical realization of the MSQs, we propose metal phthalocyanines (MPcs), which offer a range of qubit properties through choice of the metal, such as an electronic spin-1/2 with microsecond coherence times for VOPc⁷⁶ or a nuclear spin-3/2 with coherence times on the millisecond scale for TbPc₂.⁷⁷ The facile attachment of MPcs to π -conjugated surfaces such as graphene and carbon nanotubes via aromatic ligands^{26,71–75} creates supramolecular devices (Fig. 1) of itinerant electrons coupled to MSQs without fundamentally altering either.⁷¹ An alternative, but less well-studied, device might feature polynuclear single molecule magnets such as Mn₁₂ functionalized to the nanowire by electronegative ligands.^{28,78}

Chemical realization of the sd exchange intrinsically depends on the MSQ and its surface functionalization, because an electronic pathway between the itinerant electrons and MSQs

is a prerequisite for sd exchange.²⁵ For the MPc example, the spin of the Pc macrocycle couples the qubit to its environment.^{27,79–81} In the case of π -conjugated nanowires, this pathway is π -mediated.^{25,82} For the exemplary system in Fig. 1 this pathway²⁵ may stretch from MSQ ligands, to aromatic anchoring groups such as hexyl^{25,26,74} pyrenyl^{25,26,72,74,75} or its derivatives,⁸³ to the π -conjugated nanowire. An appropriate value for the coupling constant in such systems is $J_{sd} \approx 1$ meV,²⁵ many orders of magnitude smaller than the hopping amplitude in graphene.⁶³ In contrast, in our work we have set $|v|$ and J_{sd} to the same order of magnitude, which is justified in the case that the nanowire is a flat-band material, *e.g.* TBG for which a bandwidth of 4 meV⁶⁸ yields $|v| = 5$ meV in the $w = -0.4v$ case.

Inspired by the electronic properties of π -conjugated materials in supramolecular devices, to describe itinerant electrons in the nanowire we wrote down a one-dimensional tight-binding model of the Rice-Mele form that can access different regimes for the band flatness, bandgap, and density of states. However, we stress that experimental realizations of flat-band electrons are in fact more complicated than the one-dimensional tight-binding system in our simulations. For a chemical realization of the nanowire, the π -conjugated materials mentioned as ideal for MPc functionalization yield plentiful examples of flat-band physics, including TBG^{57,58} with bandwidth of a few meV,⁶⁸ zigzag SWCNTs⁶³ under a magnetic field⁶⁴ or under hydrogenation⁶⁵ with bandwidth of hundreds of meV, and doped graphene with a bandwidth about ten meV.⁶⁰ Recalling that our simulations established large density of states near the Fermi energy as the desirable property, we can tune $\rho(E_F)$ in TBGs *via* the twist angle^{57,58} or in doped graphene by substituting the dopant.⁶⁰ Likewise, SWCNTs have widely tunable band structures that can be controlled by various levers during fabrication, or *in situ* by doping or application of electric or magnetic fields.⁸⁴ For semiconducting zigzag SWCNTs, altering the hydrogenation⁶⁵ or applying a magnetic field perpendicular to the tube axis⁶⁴ enhances $\rho(E_F)$ by flattening the bands immediately above and below the Fermi energy. Alternatively, for so-called ‘metallic’ zigzag SWCNTs characterized by a band gap an order of magnitude smaller than semiconducting zigzag SWCNTs,⁸⁵ the density of

states at the Fermi energy can be enhanced linearly with the inverse tube circumference⁸⁶ or exponentially with the strength of a magnetic field applied perpendicular to the tube.^{63,87}

Conclusion

To conclude, our results show that an efficient quantum spin-valve effect occurs not only for single-electron scattering but extends to many-electron current pulses in real devices. We demonstrated that the quantum spin valve identified in Ref. 14 is recovered with many electrons as long as the density of states at the Fermi energy is enhanced (Fig. 6), which can be accomplished by detuning w (inset of Fig. 6). We used the Rice-Mele model to elucidate this essential connection between electronic properties and quantum spin valve efficiency by capturing the salient features of the first conduction and valence bands, *e.g.* bandwidth. However, the Rice-Mele model or any minimal two-band model cannot capture the full electronic structure of π -conjugated surfaces such as TBG, SWCNTs or graphene. Besides the obvious elision of bands further away from the Fermi energy, Rice-Mele fails to capture curvature effects⁶³ and the chirality of the Dirac cones.⁶⁸ An atomistic tight-binding model of the π -orbitals of the surface would provide a more sophisticated description of the electronic structure.^{57,63,68} Our survey of experimental work illustrates that candidate graphene-derived nanowires exist that can be coupled to MSQs, exhibit flat bands, and experimentally enhance $\rho(E_F)$, demonstrated in our results to correlate with an efficient quantum spin valve.

The Time-Dependent Density Matrix Renormalization Group Method

Since we aim to explore the functionality of MSQs in a current-carrying device, we have two prerogatives for our methods. First, since we are describing qubits, our methods must be fully quantum mechanical. Second, since the qubits are coupled to the nanowire for read-out, our

methods must be scalable enough to tackle this extended system. The combination of these poses a significant methodological challenge. The power of td-DMRG is that we can explore larger systems while retaining a fully quantum description of the dynamics. Many works have already taken advantage of this to investigate transport in nanoscale devices and reveal quantum effects^{43–47}. However, when it comes to entanglement, the story becomes more complicated. With continued progression towards qubit read-out, built around discrete, controllable quantum systems, it becomes increasingly important to pick out entanglement between specific, spatially differentiated subsystems. Whereas previous works only measure the entanglement that develops between all of the subsystems in aggregate, the approach we describe in Sec. incorporates from the outset the ability to resolve entanglement between any chosen degrees of freedom in the position domain. By choosing an entanglement metric with this level of spatial resolution, we capture entanglement *between each individual molecular spin along the nanowire*, and can therefore interrogate the function of these objects as qubits in a device.

Time Dependence

The starting point of time dependent DMRG is the ansatz for the many-body state, the so-called matrix product state.⁸⁸ We detail the construction and advantages of the matrix product state in the Supplementary Information. For td-DMRG, we need an efficient way to variationally minimize the many-body state, calculate expectation values from it, and unitarily time evolve it. The matrix product state unlocks this efficiency by way of its tensor structure, using matrices $\mathbf{A}^{(l)n_l}$ of dimension χ_b (referred to in the literature as the bond dimension) at each site l in the L site system to create an $\mathcal{O}(\chi_b^2 L)$ variational parameter approximation of the 4^L parameter exact many-body state. The tensor structure of the matrix product state allows efficient computation of state overlaps as well as one and two-body expectation values.⁸⁸ For variational minimization, we employ the two-site sweep algorithm⁴² from BLOCK2.⁴⁹ This consists of sweeping over subsequent pairs of matrices $\mathbf{A}^{(l)n_l} \mathbf{A}^{(l+1)n_{l+1}}$

appearing in Eq. (15) and varying the matrix elements of that pair while keeping all others fixed.^{42,89,90} Sweeping over $\mathbf{A}^{(l)n_l}\mathbf{A}^{(l+1)n_{l+1}}$ pairs remains more robust against local minima than simply varying the matrix elements of a single $\mathbf{A}^{(l)n_l}$ each time.⁴²

To evolve in time by a step dt , we operate on the matrix product state with $\exp(-i\hat{H}dt/\hbar)$. This operator must be decomposed, *e.g.* by Suzuki-Trotter.^{43,91} Suzuki-Trotter decompositions perform poorly for Hamiltonians with long-range interactions⁹² and sometimes fail to obey all conservation laws and reflect all the symmetries of the system. To remedy these deficiencies, other DMRG time evolution methods have been developed. One method is time step targeting, which expands on Suzuki-Trotter to optimize the matrix product state basis for the current time step and next time step simultaneously for more accurate treatment of long range interactions with controlled³ loss of efficiency.⁹² Another method is the time-dependent variational principle,^{44,48} which conserves energy and all other constants of motion throughout. Here, we use the time-dependent variational principle for time evolution, leading to computational complexity that scales as $\mathcal{O}(\chi_b^3)$ ⁴⁸ which happens to be the same scaling as the variational determination of the ground state matrix product state.⁴² In brief, the matrix product state is written in terms of time-dependent matrices $\mathbf{A}^{(l)n_l}(t)$ and the time-dependent variational principle dictates that the time derivatives of these matrices satisfy symplectic equations conserving all constants of motion.⁴⁸ Then, integrating these equations tells the time evolution of the state. Again, we emphasize that approximating the many-body state and time evolution with a matrix product state expands the terrain we can cover with our computational resources, as exact time evolution of a quantum system of the size and for the length of time we are interested in would be prohibitively expensive.

³Controlled in the sense that we suffer the computational cost of covering only one additional time step compared to Suzuki-Trotter.

Spatially Resolved Entanglement in td-DMRG

The matrix product state approximation of the quantum state assumes that the full system can be represented by a *pure* density matrix

$$\rho_{\text{MPS}} = |\Phi_{\text{MPS}}\rangle\langle\Phi_{\text{MPS}}| \quad (6)$$

where MPS abbreviates matrix product state. ρ_{MPS} is defined over all L orbitals of the system and can be used to compute reduced density matrices of the subsystems. The reduced density matrix of orbital 1 is defined as $\rho_1 = \text{Tr}_{2,3,4,\dots}[\rho_{\text{MPS}}]$, the reduced density matrix of orbitals 1 and 2 combined is $\rho_{12} = \text{Tr}_{3,4,\dots}[\rho_{\text{MPS}}]$, and so on. Due to interactions between the orbitals, the reduced density matrices are in general mixed even though ρ_{MPS} is pure.

The von Neumann entropy of an arbitrary (pure or mixed) density matrix ρ_{arb} is^{93–95}

$$S(\rho_{\text{arb}}) = -\text{Tr}[\rho_{\text{arb}} \ln(\rho_{\text{arb}})] = -\sum_{\alpha} \lambda_{\alpha} \ln(\lambda_{\alpha}), \quad (7)$$

where the second equality comes from extracting the eigenvalues λ_{α} from ρ_{arb} .⁹⁶ The von Neumann entropy of a density matrix quantifies the entanglement between (i) all the degrees of freedom included in that density matrix and (ii) all the other degrees of freedom of the system. It does not tell us anything about entanglement between the degrees of freedom included in the density matrix. The von Neumann entropy of a pure state is zero.

In this work, we study MSQs in the context of a current-carrying device, focusing on how the MSQ entangled states modulate the device conductance. *This requires a method powerful enough to simulate the qubits and the rest of the device interacting together, but retaining the resolution to distinguish between the qubits and the device.* Many previous applications^{43–46} of td-DMRG to the transport problem have studied the entanglement of the system as a whole, but lacked detailed exploration of the entanglement between specific subsystems. When considering MSQs in a device, these finer details are essential, as we want

to track entanglement between MSQs and avoid entangling them with the rest of the device⁴. In this section we illustrate how to quantify entanglement with this level of granularity within td-DMRG.

We now calculate the entanglement between exactly two molecular orbitals, *e.g.* $l = 1$ and $l' = 2$, of a system comprising $L > 2$ molecular orbital subsystems. This is what we mean by ‘spatially resolved entanglement,’ *i.e.* isolating the entanglement *between* a pair of degrees of freedom that differ in their spatial location, while leaving out any entanglement they may possess with the rest of the system. To do this we determine the reduced density matrices of molecular orbitals 1 and 2 (ρ_1 and ρ_2), then calculate the von Neumann entropy of these individually [$S(\rho_1)$ and $S(\rho_2)$] and jointly [$S(\rho_{12})$], and finally extract the mutual information⁹⁶

$$I(l, l') = \frac{1}{2} [S(\rho_{ll'}) - S(\rho_l) - S(\rho_{l'})] (1 - \delta_{lm}). \quad (8)$$

The mutual information is zero for unentangled subsystems and grows as the entanglement grows.

Specializing now to ρ_{MPS} , the l^{th} molecular orbital is spanned by $\{|0\rangle_l, |\uparrow\rangle_l, |\downarrow\rangle_l, |\uparrow\downarrow\rangle_l\}$ and its reduced density matrix is formally obtained as⁹⁷

$$\rho_l = \text{Tr}_{1, \dots, l-1, l+1, \dots, L} [|\Phi_{\text{MPS}}\rangle\langle\Phi_{\text{MPS}}|]. \quad (9)$$

The problem we face is that there is no way to do the required trace operations for an matrix product state. Fortunately, all the matrix elements of ρ_l can be formulated as expectation values of strings of $c_{l\sigma}^{(\dagger)}$ operators with respect to $|\Phi_{\text{MPS}}\rangle$, which are easy to compute in

⁴Sometimes, *e.g.* read-out, we do aim to entangle the MSQs with a specific subsystem. But entanglement with the rest of the device in general is always undesirable.

td-DMRG since $|\Phi_{\text{MPS}}\rangle$ is always known. This procedure yields the closed form expression⁹⁷

$$\rho_l = \text{Tr}_{1,\dots,l-1,l+1,\dots,L} [|\Phi_{\text{MPS}}\rangle\langle\Phi_{\text{MPS}}|] = \tag{10}$$

$$\begin{pmatrix} \langle\eta_{ll}\rangle & 0 & 0 & 0 \\ 0 & \langle n_{l\uparrow}(1-n_{l\downarrow})\rangle & 0 & 0 \\ 0 & 0 & \langle n_{l\downarrow}(1-n_{l\uparrow})\rangle & 0 \\ 0 & 0 & 0 & \langle n_{l\downarrow}n_{l\uparrow}\rangle \end{pmatrix} \begin{pmatrix} |0\rangle_l \\ |\uparrow\rangle_l \\ |\downarrow\rangle_l \\ |\uparrow\downarrow\rangle_l \end{pmatrix}$$

where $n_{l\sigma} \equiv c_{l\sigma}^\dagger c_{l\sigma}$ and $\eta_{ll} = (1-n_{l\downarrow})(1-n_{l\uparrow})$. In practice, we always apply this to calculate the von Neumann entropies of different MSQs along the nanowire. Since the MSQ subspace is $\{|\uparrow\rangle_d, |\downarrow\rangle_d\}$ [Eq. (16)], we only need to calculate the central 2×2 block of Eq. (10).

For two orbital reduced density matrices, we again sidestep tracing over ρ_{MPS} in favor of a closed form expression that depends only on expectation values. The expression for the full 16×16 reduced density matrix is given in given in Tables 3 and 4 of Boguslawski et al.,⁹⁶ but as with Eq. (10) we truncate from molecular orbitals to spin orbitals, yielding a 4×4 matrix with nonzero elements

$$\begin{aligned} \langle\uparrow_l\uparrow_{l'}|\rho_{l,l'}|\uparrow_l\uparrow_{l'}\rangle &= \langle(1-n_{l\downarrow})n_{l\uparrow}(1-n_{l'\downarrow})n_{l'\uparrow}\rangle \\ \langle\uparrow_l\downarrow_{l'}|\rho_{l,l'}|\uparrow_l\downarrow_{l'}\rangle &= \langle(1-n_{l\downarrow})n_{l\uparrow}(1-n_{l'\uparrow})n_{l'\downarrow}\rangle \\ \langle\uparrow_l\downarrow_{l'}|\rho_{l,l'}|\downarrow_l\uparrow_{l'}\rangle &= \langle -c_{l\downarrow}c_{l\uparrow}^\dagger c_{l'\downarrow}^\dagger c_{l'\uparrow} \rangle \\ \langle\downarrow_l\uparrow_{l'}|\rho_{l,l'}|\uparrow_l\downarrow_{l'}\rangle &= \langle -c_{l\downarrow}^\dagger c_{l\uparrow} c_{l'\uparrow} c_{l'\downarrow}^\dagger \rangle \\ \langle\downarrow_l\uparrow_{l'}|\rho_{l,l'}|\downarrow_l\uparrow_{l'}\rangle &= \langle(1-n_{l\uparrow})n_{l\downarrow}(1-n_{l'\downarrow})n_{l'\uparrow}\rangle \\ \langle\downarrow_l\downarrow_{l'}|\rho_{l,l'}|\downarrow_l\downarrow_{l'}\rangle &= \langle(1-n_{l\uparrow})n_{l\downarrow}(1-n_{l'\uparrow})n_{l'\downarrow}\rangle \end{aligned} \tag{11}$$

We use Eqs. (10)-(11) to calculate the requisite reduced density matrices and diagonalize them to find the von Neumann entropies, finally arriving at the mutual information through Eq. (8). $I(l, l')$ quantifies the spatially resolved entanglement between the different MSQs

of the system, varying from zero for unentangled MSQs to $\ln(2)$ for maximally entangled MSQs. We note that computing $\rho_{l,l'}$ in this way also enables computation of other useful metrics of qubit-qubit entanglement such as the negativity.⁹⁸

Acknowledgement

We appreciate the plentiful guidance H. Zhai and G. Chan provided so that we could fully utilize their BLOCK2 td-DMRG code.⁴⁹ We also thank A. Feiguin for many helpful discussions about td-DMRG, its strengths and weaknesses, and its application in quantum quench and quantum transport problems. This work was supported as part of the Center for Molecular Magnetic Quantum Materials, an Energy Frontier Research Center funded by the U.S. Department of Energy, Office of Science, Basic Energy Sciences under Award no. DE-SC0019330. Computations were done using the utilities of the National Energy Research Scientific Computing Center and University of Florida Research Computing and some graphics were created using Gemini.

Supporting Information Available

In the following supporting information, we give details on the Rice Mele model and explain the derivation of the matrix product state ansatz used for the td-DMRG simulations.

Rice-Mele Model

The Rice-Mele model is a minimal model of a system with two energy bands admitting a rich variety of band structures as seen in Fig. 5. In general, the Rice-Mele model consists of staggered real hopping parameters v (intracell) and w (intercell), as well as staggered intracell potential u . Rather than fitting these to real-space parameters determined, *e.g.* by a first-principles calculation, we employ Rice-Mele to theoretically model two bands two

bands near the Fermi energy. The model parameters can be set to match the shape of the bands in a real material. For example, the $w = -0.4$ valence (conduction) band depicted in Fig. 5 has its minimum (maximum) at the Γ point, and under an energy scale $|v| = 5$ meV a bandwidth of 4 meV, as reported for the two flat bands closest to the Fermi energy in twisted bilayer graphene.⁶⁸

In Eq. (2) we took $u = 0.0$, so the Rice-Mele model reduces to the Su-Schrieffer-Heeger model.⁵³ The resulting energy bands are⁵¹

$$E_{\pm}(k) = \pm\sqrt{v^2 + w^2 + 2vw \cos(ka)}, \quad (12)$$

with bandwidth $E_{\text{band}} = |w + \text{sgn}(w/v)v| - |w - \text{sgn}(w/v)v|$ and direct gap $E_{\text{gap}} = 2|w - \text{sgn}(w/v)v|$ between the (+) and (-) bands. For $\text{sgn}(w/v) = +1$ the gap is at the Brillouin zone boundary $k = \pm\pi/a$, while for $\text{sgn}(w/v) = -1$ the gap is at the Γ point. Here we fix $v = -1$ and $\text{sgn}(w/v) = +1$ while detuning w . The detuned dispersion is shown in Fig. 5. Compared to the trivial Rice-Mele limit $u = 0$, $v = w$, *i.e.* a gapless cosine band, detuning w allows us to mimic the flat-band limit of the band structure.

Matrix Product States

To construct a matrix product state (MPS), we work in the occupation number representation of a set of sites $l = 1, 2 \dots L$, where the basis states are Slater determinants $|n_1 \dots n_L\rangle$, with n_l the occupation number of the l^{th} site. In this basis we can represent any many-body state $|\Phi\rangle$ using a rank- L tensor $T^{n_1 \dots n_L}$ such that⁸⁸

$$|\Phi\rangle = \sum_{n_1 \dots n_L} T^{n_1 \dots n_L} |n_1 \dots n_L\rangle. \quad (13)$$

We can exactly transform a single rank- L tensor into a product of L rank-3 tensors according to

$$T^{n_1 \dots n_L} = \sum_{\alpha_1 \dots \alpha_L}^{\chi_e} A_{\alpha_L \alpha_1}^{(1)n_1} A_{\alpha_1 \alpha_2}^{(2)n_2} \dots A_{\alpha_{L-2} \alpha_{L-1}}^{(L-1)n_{L-1}} A_{\alpha_{L-1} \alpha_L}^{(L)n_L}, \quad (14)$$

where in addition to the occupation number indices n_l we have introduced virtual indices α_l , all of which have dimensionality χ_e . The transformation (14) is exact⁴² when $\chi_e = 4^{L/2}$ ⁵, so the complexity of $|\Phi\rangle$ scales exponentially with system size. However, truncating the dimensionality of the virtual indices to the so-called bond dimension $\chi_b \ll \chi_e$ makes the product tractable.⁴³ We are left with the nonlinear variational MPS⁶

$$|\Phi_{\text{MPS}}\rangle = \sum_{n_1 \dots n_L} \sum_{\alpha_1 \dots \alpha_L}^{\chi_b} A_{\alpha_1}^{(1)n_1} A_{\alpha_1 \alpha_2}^{(2)n_2} \dots A_{\alpha_{L-1}}^{(L)n_L} |n_1 \dots n_L\rangle. \quad (15)$$

$|\Phi_{\text{MPS}}\rangle$ possesses only $\mathcal{O}(\chi_b^2 L)$ matrix elements,^{42,88} as opposed to the exponentially scaling $\mathcal{O}(4^L)$ matrix elements in the exact $|\Phi\rangle$, but by harnessing the principle of locality it achieves controlled accuracy with increasing χ_b .^{43,88}

The fundamental objects of $|\Phi_{\text{MPS}}\rangle$ are the matrices $\mathbf{A}^{(l)n_l}$ whose matrix elements, indexed by α_l , are the variational parameters^{42,88} encoding physical correlations between different sites. $|\Phi_{\text{MPS}}\rangle$ can encode more correlations between sites whose corresponding matrices contract over a shared α_l , so assigning an order $l = 1, 2, \dots, L$ to the sites impacts the results. In other words, the MPS ansatz assumes a 1D structure to the physical correlation and imposes this through the site ordering. This makes site ordering straightforward for 1D or nearly 1D systems (*e.g.* nanowires) and explains why td-DMRG is best applied to such systems.⁴² For non-1D systems ordering the sites to optimize accuracy is challenging.^{42,88} In our case, the sites discretizing the nanowire are already 1D. To handle the MSQ degrees of freedom without sacrificing our 1D geometry, we take each site in the scattering region unit

⁵This holds for molecular orbitals where $n_l \in \{0, \uparrow_l, \downarrow_l, 2_l\}$ ⁸⁸ while for spin orbitals or qubit systems $n_l \in \{0, 1\}$ and $\chi_e = 2^{L/2}$.

⁶Following the convention, we dropped the contraction over α_L between $\mathbf{A}^{(1)n_1}$ and $\mathbf{A}^{(L)n_L}$.

cells $N_L \leq j \leq N_L + N_{FM} - 1$, *i.e.* all the sites exchange coupled to the MSQs by Eq. (2), and expand their local Hilbert space from purely fermionic

$$\{|0\rangle_{j\mu}, |\uparrow\rangle_{j\mu}, |\downarrow\rangle_{j\mu}, |\uparrow\downarrow\rangle_{j\mu}\}$$

to encompass the MSQ degrees of freedom:

$$\{|0\rangle_{j\mu}, |\uparrow\rangle_{j\mu}, |\downarrow\rangle_{j\mu}, |\uparrow\downarrow\rangle_{j\mu}\} \otimes \{|\uparrow\rangle_d, |\downarrow\rangle_d\}, \quad (16)$$

a process known as ‘supersiting.’

Time Evolution of Finite Quantum Systems

While the td-DMRG method unlocks access to more complicated systems with more itinerant electrons, we are still simulating finite systems and must consider finite size effects. This is a notable departure from the methods of Ciccarello,^{14,99} who describe infinite leads at the cost of handling only one itinerant electron. In particular, our system contains N_{total} sites, with the itinerant electrons starting in the leftmost of these and moving rightwards over time. The onset of finite size effects comes when the nanowire’s right boundary at $j = N_{\text{total}} - 1$ backscatters the electrons,⁴³ at the time we label t_{fin} . Prior to t_{fin} , the transport of electrons across the scattering region faithfully describes the dynamics of electrons in an open nanowire⁴³ and can approximate steady-state transport quantities.⁴⁷

We quantify t_{fin} using the time-dependent occupation of the right boundary unit cell,

$$n_{\text{bdy}}(t) = \sum_{\mu} \sum_{\sigma} \langle c_{j\mu\sigma}^{\dagger} c_{j\mu\sigma} \rangle_{j=N_{\text{total}}-1}. \quad (17)$$

Initially, this occupation monotonically increases due to the (physically normal) rightward electron flow. However, backscattering turns on (unphysical, caused by finite-size) leftward

reflection that will eventually cancel out the rightward flow. This marks the presence of finite-size effects and allows us to define t_{fin} as

$$\frac{d}{dt}n_{\text{bdy}}(t_{\text{fin}}) = 0. \quad (18)$$

Fig. 9 shows the determination of t_{fin} for the $w = -0.40$ simulations. Note that we assign t_{fin} to the discrete t value closest to (18).

Single-Particle Eigenstates

For $t < 0$ Hamiltonian contains no interaction between the MSQs and itinerant electrons, so $\hat{H}(t < 0)$ can be broken into a part acting on MSQs [the last line of Eq. (3)] and a part acting on itinerant electrons [the v and w terms in Eq. (2) and the first line of Eq. (3)]. The electronic part of $\hat{H}(t < 0)$ commutes with the electron momentum operator as well as the electron spin in the z -direction $\sum_{j\mu}(c_{j\mu\uparrow}^\dagger c_{j\mu\uparrow} - c_{j\mu\downarrow}^\dagger c_{j\mu\downarrow})/2$, so we label the m^{th} $t < 0$ single-particle eigenstate $|k_m\sigma_e^m\rangle$, where $\hbar k_m$ is the momentum of the state and $\sigma_e^m = \pm\hbar/2$ is the projection of its spin along the z -axis. Analogously to the Bloch states propagating in the crystal lattice of a metal or semiconductor, the single-particle eigenstates $|k_m\sigma_e^m\rangle$ are the modes through which the itinerant electrons propagate along the nanowire. The energy eigenvalues E of these eigenstates are discrete due to the finite size of the system, but still satisfy the Rice-Mele dispersion [Eq. (12)] from which follows the density of states

$$\rho(E) = 2/\pi|dE/dk_m|. \quad (19)$$

Under Eq. (2) the energies are independent of σ_e^m and so twofold degenerate. The occupation function for a spin-unpolarized system (N_e even) is

$$n_m(E) = \begin{cases} 2 & m \leq N_e \\ 0 & m > N_e \end{cases} \quad (20)$$

and the Fermi energy is $E_F = E_{N_e}$. From the single-particle eigenstates we can construct the $t < 0$ many-body state

$$|\Psi(t < 0)\rangle = |n_1 \dots n_m \dots\rangle \otimes |\psi_{\text{qubit}}\rangle \quad (21)$$

where $|n_1 \dots n_m \dots\rangle$ is a Slater determinant in the occupation number representation of the single-particle eigenstates and $|\psi_{\text{qubit}}\rangle$ is a maximally entangled state of the form (1). Note that \hat{H}_0 dictates the phase of $|\psi_{\text{qubit}}\rangle$ according to

$$\phi_{\text{ent}} = \cos^{-1} \left(J_{\text{ent}} / \sqrt{J_{\text{ent}}^2 + J_{\text{ent}}'^2} \right) \quad (22)$$

and that ϕ_{ent} can be read from the observable

$$\langle \psi_{\text{qubit}} | (\mathbf{S}_1 + \mathbf{S}_2)^2 | \psi_{\text{qubit}} \rangle = 1 + \cos(\phi_{\text{ent}}). \quad (23)$$

The $t < 0$ many-body state $|\Psi(t < 0)\rangle$ is a key variable in our simulations, determining the energies and momenta of the electrons during the transport. We depict $|\Psi(t < 0)\rangle$ in real space in Fig. 10 and in energy space in Fig. 5. In the latter, we observe how detuning w changes the electronic properties, gapping the single-particle eigenstates and narrowing the bandwidth to $E_{\text{band}} = 0.8$. In general we expect the quantum spin valve efficiency to vary with these electronic properties¹⁴. The full distribution of single-particle energies and momenta can be seen in Fig. 5. A simple, physical way to describe the single-particle eigenstates as we change $|\Psi(t < 0)\rangle$ by detuning w is the density of states at the Fermi

energy $\rho(E_F)$, which tells us about the propagation of the highest energy itinerant electron. The momentum of a given electron is inversely proportional to its density of states, and when $\rho(E_F)$ is small we expect faster propagating electrons. For fixed N_e , $\rho(E_F)$ has a one-to-one correspondence with w as seen the inset of Fig. 6 where decreasing w increases $\rho(E_F)$ and flattens the band. The Rice-Mele hopping w therefore serves as a knob in the Hamiltonian that we can use to engineer desirable electronic properties, such as enhanced $\rho(E_F)$.

Code Availability

Full td-DMRG code used in all simulations available upon request.

References

1. Michael Nielsen and Isaac Chuang *Quantum Computation and Quantum Information: 10th Anniversary Edition*; Cambridge University Press: Cambridge, 2011.
2. Charles H. Bennett and David P. DiVincenzo Quantum information and computation. *Nature* **2000**, *404*, 247–255.
3. Daniel Loss and David P. DiVincenzo Quantum computation with quantum dots. *Phys. Rev. A* **1998**, *57*, 120–126.
4. Burkard, G.; Ladd, T. D.; Pan, A.; Nichol, J. M.; Petta, J. R. Semiconductor spin qubits. *Rev. Mod. Phys.* **2023**, *95*, 025003.
5. Matteo Atzori and Roberta Sessoli The Second Quantum Revolution: Role and Challenges of Molecular Chemistry. *J. Am. Chem. Soc.* **2019**, *141*, 11339–11352.
6. A. Gaita-Ariño, F. Luis, S. Hill, E. Coronado Molecular spins for quantum computation. *Nature Chemistry* **2019**, *11*, 301–309.

7. Michael N. Leuenberger and Daniel Loss Quantum computing in molecular magnets. *Nature* **2001**, *410*, 789–793.
8. Brian Sutton and Supriyo Datta Manipulating quantum information with spin torque. *Sci Rep* **2016**, *5*, 17912.
9. A. T. Costa, Jr., S. Bose, Y. Omar Entanglement of Two Impurities through Electron Scattering. *Phys. Rev. Lett.* **2006**, *96*, 230501.
10. Francesco Ciccarello, G. Massimo Palma, Mauro Paternostro, Michelangelo Zarcone, Yasser Omar Entanglement generation between two spin-s magnetic impurities in a solid via electron scattering. *Solid State Sciences* **2009**, *11*, 931–934.
11. K. Yuasa, H. Nakazato Resonant scattering can enhance the degree of entanglement. *J. Phys. A: Math. Theor.* **2006**, *40*, 297–308.
12. Kazuya Yuasa, Daniel Burgarth, Vittorio Giovannetti and Hiromichi Nakazato Efficient generation of a maximally entangled state by repeated on- and off-resonant scattering of ancilla qubits. *New Journal of Physics* **2009**, *11*, 123027.
13. Christian Bunker, Silas Hoffman, Jie-Xiang Yu, Xiao-Guang Zhang, and Hai-Ping Cheng Scattering solution of an interacting Hamiltonian for the electronic control of molecular spin qubits. *Phys. Rev. A* **2023**, *107*, 042423.
14. Francesco Ciccarello, Massimo Palma, Michelangelo Zarcone, Yasser Omar, Vitor Rocha Vieira Entanglement controlled single-electron transmittivity. *New J. Phys.* **2006**, *8*, 214.
15. Wolfgang Pfaff, Tim H. Taminiau, Lucio Robledo, Hannes Bernien, Matthew Markham, Daniel J. Twitchen & Ronald Hanson Demonstration of entanglement-by-measurement of solid-state qubits. *Nature Phys.* **2013**, *9*, 29–33.

16. Jörg Lehmann, Alejandro Gaita-Arino, Eugenio Coronado and Daniel Loss Spin qubits with electrically gated polyoxometalate molecules. *Nature Nanotech.* **2007**, *2*, 312–317.
17. Clement Godfrin, Stefan Thiele, Abdelkarim Ferhat, Svetlana Klyatskaya, Mario Ruben, Wolfgang Wernsdorfer, and Franck Balestro Electrical Read-Out of a Single Spin Using an Exchange-Coupled Quantum Dot. *ACS Nano* **2017**, *11*, 3984–3989.
18. M. Veldhorst, H. G. J. Eenink, C. H. Yang & A. S. Dzurak Silicon CMOS architecture for a spin-based quantum computer. *Nat. Commun.* **2017**, *8*, 1766.
19. Will Gilbert *et al.* On-demand electrical control of spin qubits. *Nat. Nanotechnol.* **2023**, *18*, 131–136.
20. A. M. J. Zwerver *et al.* Qubits made by advanced semiconductor manufacturing. *Nature Electronics* **2022**, *5*, 184–190.
21. Petta, J. R.; Johnson, A. C.; Taylor, J. M.; Laird, E. A.; Yacoby, A.; Lukin, M. D.; Marcus, C. M.; Hanson, M. P.; Gossard, A. C. Coherent Manipulation of Coupled Electron Spins in Semiconductor Quantum Dots. *Science* **2005**, *309*.
22. Takashi Nakajima *et al.* Robust Single-Shot Spin Measurement with 99.5% Fidelity in a Quantum Dot Array. *Phys. Rev. Lett.* **2017**, *119*.
23. Connors, E. J.; Nelson, J.; Nichol, J. M. Rapid High-Fidelity Spin-State Readout in Si/Si-Ge Quantum Dots via rf Reflectometry. *Phys. Rev. Appl.* **2020**, *13*.
24. Maune, B.; Borselli, M. G.; Huang, B.; Ladd, T. D.; Deelman, P. W.; Holabird, K. S.; Kiselev, A. A.; Alvarado-Rodriguez, I.; Ross, R. S.; Schmitz, A. E.; Sokolich, M.; Watson, C. A.; Gyure, M. F.; Hunter, A. T. Coherent singlet-triplet oscillations in a silicon-based double quantum dot. *Nature* **2012**, *481*.
25. M. Urdampilleta, S. Klyatskaya, J-P. Cleuziou, M. Ruben, and W. Wernsdorfer Supramolecular spin valves. *Nature Mater.* **2011**, *10*, 502–506.

26. Candini, A.; Klyatskaya, S.; Ruben, M.; Wernsdorfer, W.; Affronte, M. Graphene Spintronic Devices with Molecular Nanomagnets. *Nano Letters* **2011**, *11*, 2634–2639.
27. Krainov, I. V.; Klier, J.; Dmitriev, A. P.; Klyatskaya, S.; Ruben, M.; Wernsdorfer, W.; Gornyi, I. V. Giant Magnetoresistance in Carbon Nanotubes with Single-Molecule Magnets TbPc2. *ACS Nano* **2017**, *11*, 6868–6880, PMID: 28613829.
28. Amjad Alqahtani et al. Electrical Detection of Magnetization Switching in Single-Molecule Magnets, Ver. 1. *arXiv* July 30, 2024. DOI:10.48550/arXiv.2407.21156.
29. J. R. Schrieffer and P. A. Wolff Relation between the Anderson and Kondo Hamiltonians. *Phys. Rev.* **1966**, *149*, 491.
30. Eric D. Switzer, Xiao-Guang Zhang, Talat S. Rahman Anisotropy-Exchange Resonance as a Mechanism for Entangled State Switching. *Phys. Rev. A* **2021**, *104*, 052434.
31. J. Kondo Resistance Minimum in Dilute Magnetic Alloys. *Prog. Theor. Phys.* **1964**, *32*, 37–49.
32. A. C. Hewson *The Kondo Problem to Heavy Fermions*; Cambridge University Press: Cambridge, 1993.
33. Francesco Ciccarello and G Massimo Palma and Michelangelo Zarcone and Yasser Omar and Vitor R Vieira Electron Fabry–Perot interferometer with two entangled magnetic impurities. *Journal of Physics A: Mathematical and Theoretical* **2007**, *40*.
34. Sharma, A.; Tulapurkar, A. A. Transmission-based tomography for spin qubits. *Phys. Rev. A* **2021**, *103*.
35. Dieny, B.; Speriosu, V. S.; Parkin, S. S. P.; Gurney, B. A.; Wilhoit, D. R.; Mauri, D. Giant magnetoresistive in soft ferromagnetic multilayers. *Phys. Rev. B* **1991**, *43*, 1297–1300.

36. Binasch, G.; Grünberg, P.; Saurenbach, F.; Zinn, W. Enhanced magnetoresistance in layered magnetic structures with antiferromagnetic interlayer exchange. *Phys. Rev. B* **1989**, *39*, 4828–4830.
37. Chappert, C.; Fert, A.; Dau, F. N. V. The emergence of spin electronics in data storage. *Nature Materials* **2007**, *6*, 813–823.
38. Baltz, V.; Manchon, A.; Tsoi, M.; Moriyama, T.; Ono, T.; Tserkovnyak, Y. Antiferromagnetic spintronics. *Rev. Mod. Phys.* **2018**, *90*, 015005.
39. Bordoloi, A.; Zannier, V.; Sorba, L.; Schönenberger, C.; Baumgartner, A. A double quantum dot spin valve. *Commun Phys* **2020**, *3*, 135.
40. Schollwöck, U. The density-matrix renormalization group. *Rev. Mod. Phys.* **2005**, *77*, 259–315.
41. Schollwöck, U. The density-matrix renormalization group in the age of matrix product states. *Annals of Physics* **2011**, *326*, 96–192.
42. Olivares-Amaya, R.; Hu, W.; Nakatani, N.; Sharma, S.; Yang, J.; Chan, G. K.-L. The ab-initio density matrix renormalization group in practice. *The Journal of Chemical Physics* **2015**, *142*, 034102.
43. Petrović, M. D.; Mondal, P.; Feiguin, A. E.; Plecháč, P.; Nikolić, B. K. Spintronics Meets Density Matrix Renormalization Group: Quantum Spin-Torque-Driven Nonclassical Magnetization Reversal and Dynamical Buildup of Long-Range Entanglement. *Phys. Rev. X* **2021**, *11*, 021062.
44. Yang, H.; Li, W.; Ren, J.; Shuai, Z. Time-Dependent Density Matrix Renormalization Group Method for Quantum Transport with Phonon Coupling in Molecular Junction. *Journal of Chemical Theory and Computation* **2023**, *19*, 6070–6081.

45. Chung, C.-M.; Wauters, M. M.; Burrello, M. Matrix product state simulations of quantum quenches and transport in Coulomb blockaded superconducting devices. *Phys. Rev. B* **2022**, *106*, 094308.
46. Dias da Silva, L. G. G. V.; Heidrich-Meisner, F.; Feiguin, A. E.; Büsser, C. A.; Martins, G. B.; Anda, E. V.; Dagotto, E. Transport properties and Kondo correlations in nanostructures: Time-dependent DMRG method applied to quantum dots coupled to Wilson chains. *Phys. Rev. B* **2008**, *78*, 195317.
47. Al-Hassanieh, K. A.; Feiguin, A. E.; Riera, J. A.; Büsser, C. A.; Dagotto, E. Adaptive time-dependent density-matrix renormalization-group technique for calculating the conductance of strongly correlated nanostructures. *Phys. Rev. B* **2006**, *73*, 195304.
48. Haegeman, J.; Cirac, J. I.; Osborne, T. J.; Pižorn, I.; Verschelde, H.; Verstraete, F. Time-Dependent Variational Principle for Quantum Lattices. *Phys. Rev. Lett.* **2011**, *107*, 070601.
49. H. Zhai et al. Block2: A comprehensive open source framework to develop and apply state-of-the-art DMRG algorithms in electronic structure and beyond. *The Journal of Chemical Physics* **2023**, *159*, 234801.
50. János K. Asbóth, László Oroszlány, András Pályi *A Short Course on Topological Insulators*; Springer, 2016.
51. Lin, Y.-T. Functional renormalization group study on interacting gapped systems with topological properties. Ph.D. thesis, Aachen University, 2022.
52. Rice, M. J.; Mele, E. J. Elementary Excitations of a Linearly Conjugated Diatomic Polymer. *Phys. Rev. Lett.* **1982**, *49*, 1455–1459.
53. Su, W. P.; Schrieffer, J. R.; Heeger, A. J. Solitons in Polyacetylene. *Phys. Rev. Lett.* **1979**, *42*, 1698–1701.

54. Hu, G.; Guo, Y.; Wei, J.; Xie, S. Spin filtering through a metal/organic-ferromagnet/metal structure. *Phys. Rev. B* **2007**, *75*, 165321.
55. Kim, K. K.; Kim, S. M.; Lee, Y. H. Chemically Conjugated Carbon Nanotubes and Graphene for Carrier Modulation. *Accounts of Chemical Research* **2016**, *49*, 390–399, PMID: 26878595.
56. Derzhko, O.; Richter, J.; Maksymenko, M. Strongly correlated flat-band systems: The route from Heisenberg spins to Hubbard electrons. *International Journal of Modern Physics B* **2015**, *29*, 1530007.
57. Bistritzer, R.; MacDonald, A. H. Moiré bands in twisted double-layer graphene. *Proceedings of the National Academy of Sciences* **2011**, *108*.
58. Andrei, E. Y.; MacDonald, A. H. Graphene bilayers with a twist. *Nature Materials* **2020**, *19*.
59. Suárez Morell, E.; Vergara, R.; Pacheco, M.; Brey, L.; Chico, L. Electronic properties of twisted bilayer nanoribbons. *Phys. Rev. B* **2014**, *89*, 205405.
60. Ehlen, N.; Hell, M.; Marini, G.; Hasdeo, E. H.; Saito, R.; Falke, Y.; Goerbig, M. O.; Di Santo, G.; Petaccia, L.; Profeta, G.; Grüneis, A. Origin of the Flat Band in Heavily Cs-Doped Graphene. *ACS Nano* **2020**, *14*, 1055–1069, PMID: 31825586.
61. Henck, H.; Avila, J.; Ben Aziza, Z.; Pierucci, D.; Baima, J.; Pamuk, B.; Chaste, J.; Utt, D.; Bartos, M.; Nogajewski, K.; Piot, B. A.; Orlita, M.; Potemski, M.; Calandra, M.; Asensio, M. C.; Mauri, F.; Faugeras, C.; Ouerghi, A. Flat electronic bands in long sequences of rhombohedral-stacked graphene. *Phys. Rev. B* **2018**, *97*, 245421.
62. Pierucci, D.; Sediri, H.; Hajlaoui, M.; Girard, J.-C.; Brumme, T.; Calandra, M.; Velez-Fort, E.; Patriarche, G.; Silly, M. G.; Ferro, G.; Soulière, V.; Marangolo, M.; Sirotti, F.;

- Mauri, F.; Ouerghi, A. Evidence for Flat Bands near the Fermi Level in Epitaxial Rhombohedral Multilayer Graphene. *ACS Nano* **2015**, *9*, 5432–5439, PMID: 25893537.
63. Charlier, J.-C.; Blase, X.; Roche, S. Electronic and transport properties of nanotubes. *Rev. Mod. Phys.* **2007**, *79*, 677–732.
64. Saito, R.; Dresselhaus, G.; Dresselhaus, M. S. Magnetic energy bands of carbon nanotubes. *Phys. Rev. B* **1994**, *50*, 14698–14701.
65. Yang, X.; Wu, G. Itinerant Flat-Band Magnetism in Hydrogenated Carbon Nanotubes. *ACS Nano* **2009**, *3*, 1646–1650, PMID: 19548640.
66. Mitra, A. Quantum Quench Dynamics. *Annual Review of Condensed Matter Physics* **2018**, *9*, 245–259.
67. Veldman, L. M.; Farinacci, L.; Rejali, R.; Broekhoven, R.; Gobeil, J.; Coffey, D.; Ternes, M.; Otte, A. F. Free coherent evolution of a coupled atomic spin system initialized by electron scattering. *Science* **2021**, *372*, 964–968.
68. Po, H. C.; Zou, L.; Senthil, T.; Vishwanath, A. Faithful tight-binding models and fragile topology of magic-angle bilayer graphene. *Phys. Rev. B* **2019**, *99*, 195455.
69. Romain Vincent, Svetlana Klyatskaya, Mario Ruben, Wolfgang Wernsdorfer & Franck Balestro Electronic read-out of a single nuclear spin using a molecular spin transistor. *Nature* **2012**, *488*, 357–360.
70. Stefan Thiele, Franck Balestro, Rafik Ballou, Svetlana Klyatskaya, Mario Ruben, Wolfgang Wernsdorfer Electrically driven nuclear spin resonance in single-molecule magnets. *Science* **2014**, *344*, 1135–1138.
71. Bottari, G.; de la Torre, G.; Guldi, D. M.; Torres, T. Covalent and Noncovalent Phthalocyanine-Carbon Nanostructure Systems: Synthesis, Photoinduced Electron

- Transfer, and Application to Molecular Photovoltaics. *Chemical Reviews* **2010**, *110*, 6768–6816, PMID: 20364812.
72. Kyatskaya, S.; Galán Mascarós, J. R.; Bogani, L.; Hennrich, F.; Kappes, M.; Wernsdorfer, W.; Ruben, M. Anchoring of Rare-Earth-Based Single-Molecule Magnets on Single-Walled Carbon Nanotubes. *Journal of the American Chemical Society* **2009**, *131*, 15143–15151, PMID: 19799421.
73. Wang, Y.; Hu, N.; Zhou, Z.; Xu, D.; Wang, Z.; Yang, Z.; Wei, H.; Kong, E. S.-W.; Zhang, Y. Single-walled carbon nanotube/cobalt phthalocyanine derivative hybrid material: preparation, characterization and its gas sensing properties. *J. Mater. Chem.* **2011**, *21*, 3779–3787.
74. Lopes, M.; Candini, A.; Urdampilleta, M.; Reserbat-Plantey, A.; Bellini, V.; Klyatskaya, S.; Marty, L.; Ruben, M.; Affronte, M.; Wernsdorfer, W.; Bendiab, N. Surface-Enhanced Raman Signal for Terbium Single-Molecule Magnets Grafted on Graphene. *ACS Nano* **2010**, *4*, 7531–7537, PMID: 21067149.
75. Bartelmess, J.; Ballesteros, B.; de la Torre, G.; Kiessling, D.; Campidelli, S.; Prato, M.; Torres, T.; Guldi, D. M. Phthalocyanine-Pyrene Conjugates: A Powerful Approach toward Carbon Nanotube Solar Cells. *Journal of the American Chemical Society* **2010**, *132*, 16202–16211, PMID: 20973540.
76. Atzori, M.; Tesi, L.; Morra, E.; Chiesa, M.; Sorace, L.; Sessoli, R. Room-Temperature Quantum Coherence and Rabi Oscillations in Vanadyl Phthalocyanine: Toward Multifunctional Molecular Spin Qubits. *Journal of the American Chemical Society* **2016**, *138*, 2154–2157, PMID: 26853512.
77. Godfrin, C.; Ferhat, A.; Ballou, R.; Klyatskaya, S.; Ruben, M.; Wernsdorfer, W.; Balestro, F. Operating Quantum States in Single Magnetic Molecules: Implementation of Grover’s Quantum Algorithm. *Phys. Rev. Lett.* **2017**, *119*, 187702.

78. Zhu, X.; Hale, A.; Christou, G.; Hebard, A. F. Electronegative ligands enhance charge transfer to Mn12 single-molecule magnets deposited on graphene. *Journal of Applied Physics* **2020**, *127*, 064303.
79. Urdampilleta, M.; Klyatskaya, S.; Ruben, M.; Wernsdorfer, W. Landau-Zener tunneling of a single Tb³⁺ magnetic moment allowing the electronic read-out of a nuclear spin. *Phys. Rev. B* **2013**, *87*, 195412.
80. Lodi Rizzini, A.; Krull, C.; Balashov, T.; Kavich, J. J.; Mugarza, A.; Miedema, P. S.; Thakur, P. K.; Sessi, V.; Klyatskaya, S.; Ruben, M.; Stepanow, S.; Gambardella, P. Coupling Single Molecule Magnets to Ferromagnetic Substrates. *Phys. Rev. Lett.* **2011**, *107*, 177205.
81. Komeda, T., Isshiki, H., Liu, J. et al. Observation and electric current control of a local spin in a single-molecule magnet. *Nat. Commun.* **2011**, *2*, 217.
82. Marocchi, S.; Candini, A.; Klar, D.; Van den Heuvel, W.; Huang, H.; Troiani, F.; Corradini, V.; Biagi, R.; De Renzi, V.; Klyatskaya, S.; Kummer, K.; Brookes, N. B.; Ruben, M.; Wende, H.; del Pennino, U.; Soncini, A.; Affronte, M.; Bellini, V. Relay-Like Exchange Mechanism through a Spin Radical between TbPc2 Molecules and Graphene/Ni(111) Substrates. *ACS Nano* **2016**, *10*, 9353–9360, PMID: 27726335.
83. Chitta, R.; Sandanayaka, A. S. D.; Schumacher, A. L.; D'Souza, L.; Araki, Y.; Ito, O.; D'Souza, F. Donor-Acceptor Nanohybrids of Zinc Naphthalocyanine or Zinc Porphyrin Noncovalently Linked to Single-Wall Carbon Nanotubes for Photoinduced Electron Transfer. *The Journal of Physical Chemistry C* **2007**, *111*, 6947–6955.
84. Qian, L.; Xie, Y.; Zhang, S.; Zhang, J. Band Engineering of Carbon Nanotubes for Device Applications. *Matter* **2020**, *3*, 664–695.
85. Ouyang, M.; Huang, J.-L.; Cheung, C. L.; Lieber, C. M. Energy Gaps in "Metallic" Single-Walled Carbon Nanotubes. *Science* **2001**, *292*, 702–705.

86. Mintmire, J. W.; White, C. T. Universal Density of States for Carbon Nanotubes. *Phys. Rev. Lett.* **1998**, *81*, 2506–2509.
87. Ando, T.; Seri, T. Quantum Transport in a Carbon Nanotube in Magnetic Fields. *Journal of the Physical Society of Japan* **1997**, *66*, 3558–3565.
88. Chan, G. K.-L.; Sharma, S. The Density Matrix Renormalization Group in Quantum Chemistry. *Annual Review of Physical Chemistry* **2011**, *62*, 465–481.
89. White, S. R. Density-matrix algorithms for quantum renormalization groups. *Phys. Rev. B* **1993**, *48*, 10345–10356.
90. Density Matrix Renormalization Group Algorithm (DMRG). <http://tensornetwork.org/mps/algorithms/dmrg/>, February 26, 2026; Accessed: 11-29-2024.
91. White, S. R.; Feiguin, A. E. Real-Time Evolution Using the Density Matrix Renormalization Group. *Phys. Rev. Lett.* **2004**, *93*, 076401.
92. Feiguin, A. E.; White, S. R. Time-step targeting methods for real-time dynamics using the density matrix renormalization group. *Phys. Rev. B* **2005**, *72*, 020404.
93. Legeza, O.; Sólyom, J. Optimizing the density-matrix renormalization group method using quantum information entropy. *Phys. Rev. B* **2003**, *68*, 195116.
94. William Wootters Entanglement of Formation and Concurrence. *Quantum Information and Computation* **2001**, *1*, 27–44.
95. William Wootters Entanglement of Formation of an Arbitrary State of Two Qubits. *Phys Rev Lett* **1998**, *80*, 2245–2248.
96. Katharina Boguslawski, Pawel Tecmer, Gergely Barcza, Örs Legeza, Markus Reiher Orbital Entanglement in Bond-Formation Processes. *Journal of Chemical Theory and Computation* **2013**, *9*, 2959–2973.

97. Rissler, J.; Noack, R. M.; White, S. R. Measuring orbital interaction using quantum information theory. *Chemical Physics* **2006**, *323*, 519–531.
98. Vidal, G.; Werner, R. F. Computable measure of entanglement. *Phys. Rev. A* **2002**, *65*, 032314.
99. O. L. T. de Menezes, J. S. Helman Spin flip enhancement at resonant transmission. *Am. J. Phys.* **1985**, *53*, 1100–1102.

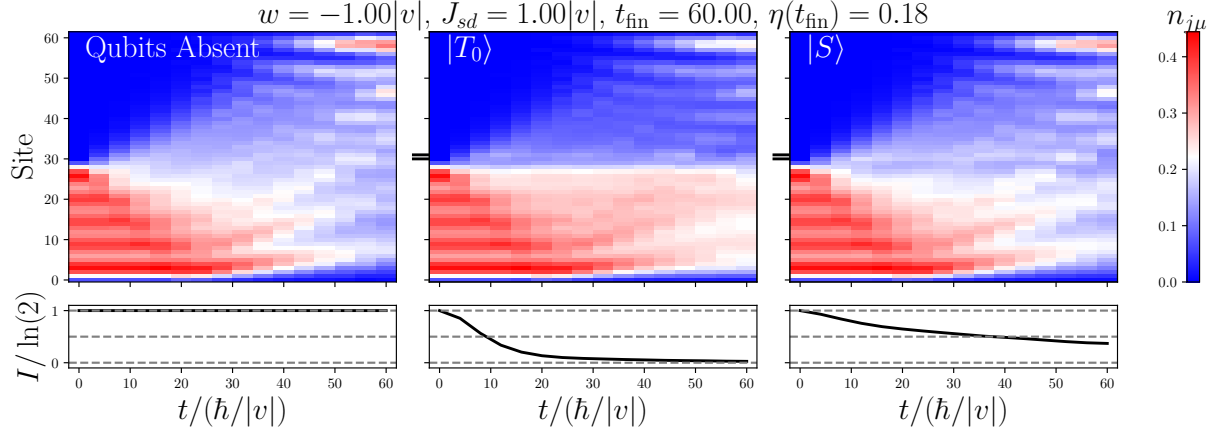


Figure 3: Panels show simulations of a system without MSQs, with $|T_0\rangle$ MSQs, and with $|S\rangle$ MSQs. Upper plot of each panel: color shows the electronic occupation $n_{j\mu}$ of a given site at a given time. The sites $|j\mu\rangle$ discretizing the 1D chain are along the vertical axis while time t , measured in units $\hbar/|v|$, is along the horizontal axis. Lower plot of each panel: perturbation of the MSQ entanglement, quantified by I [Eq. (8)]. Hamiltonian parameters are $w = -1.00$, $J_{sd} = 1.00$, $N_e = 10$, geometric parameters are $N_L = N_R = 15$, $N_{\text{total}} = 31$, and td-DMRG parameters are $\chi_b = 250$, $dt = 0.1$.

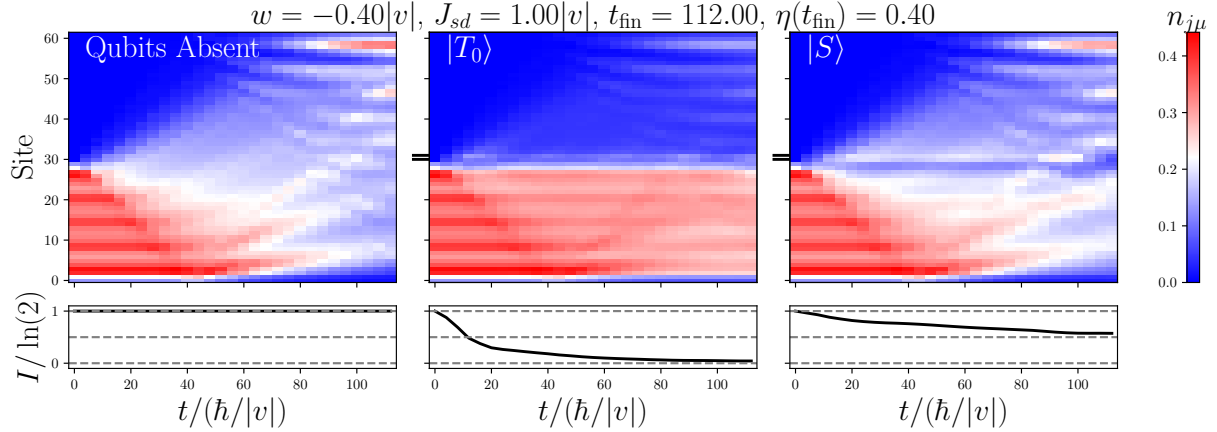


Figure 4: Panels show simulations of a system without MSQs, with $|T_0\rangle$ MSQs, and with $|S\rangle$ MSQs. Upper plot of each panel: color shows the electronic occupation $n_{j\mu}$ of a given site at a given time. The sites $|j\mu\rangle$ discretizing the 1D chain are along the vertical axis while time t , measured in units $\hbar/|v|$, is along the horizontal axis. Lower plot of each panel: perturbation of the MSQ entanglement, quantified by I [Eq. (8)]. Notice the jump in quantum spin valve efficiency η obtained by detuning w from $w = -1.00$ to $w = -0.40$. Parameters besides w are the same as Fig. 3.

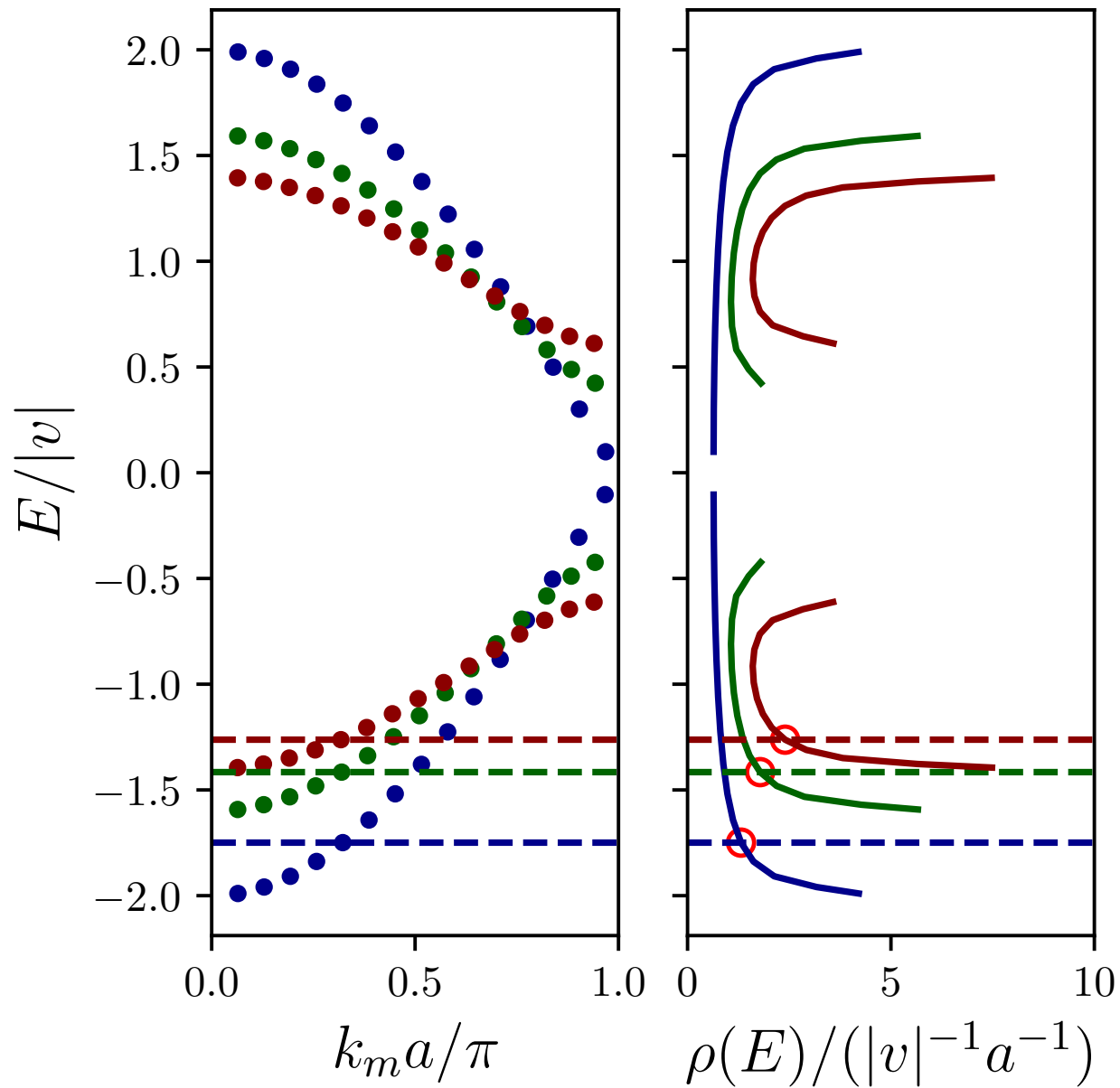


Figure 5: Discrete $t > 0$ single-particle energy eigenstates E and associated wavenumbers k_m and density of states $\rho(E)$. Spectrum computed for $w = -1$ (blue), $w = -0.60$ (green) and $w = -0.40$ (red) Rice-Mele bands. Dashed lines show Fermi energy E_F and red circles show $\rho(E_F)$.

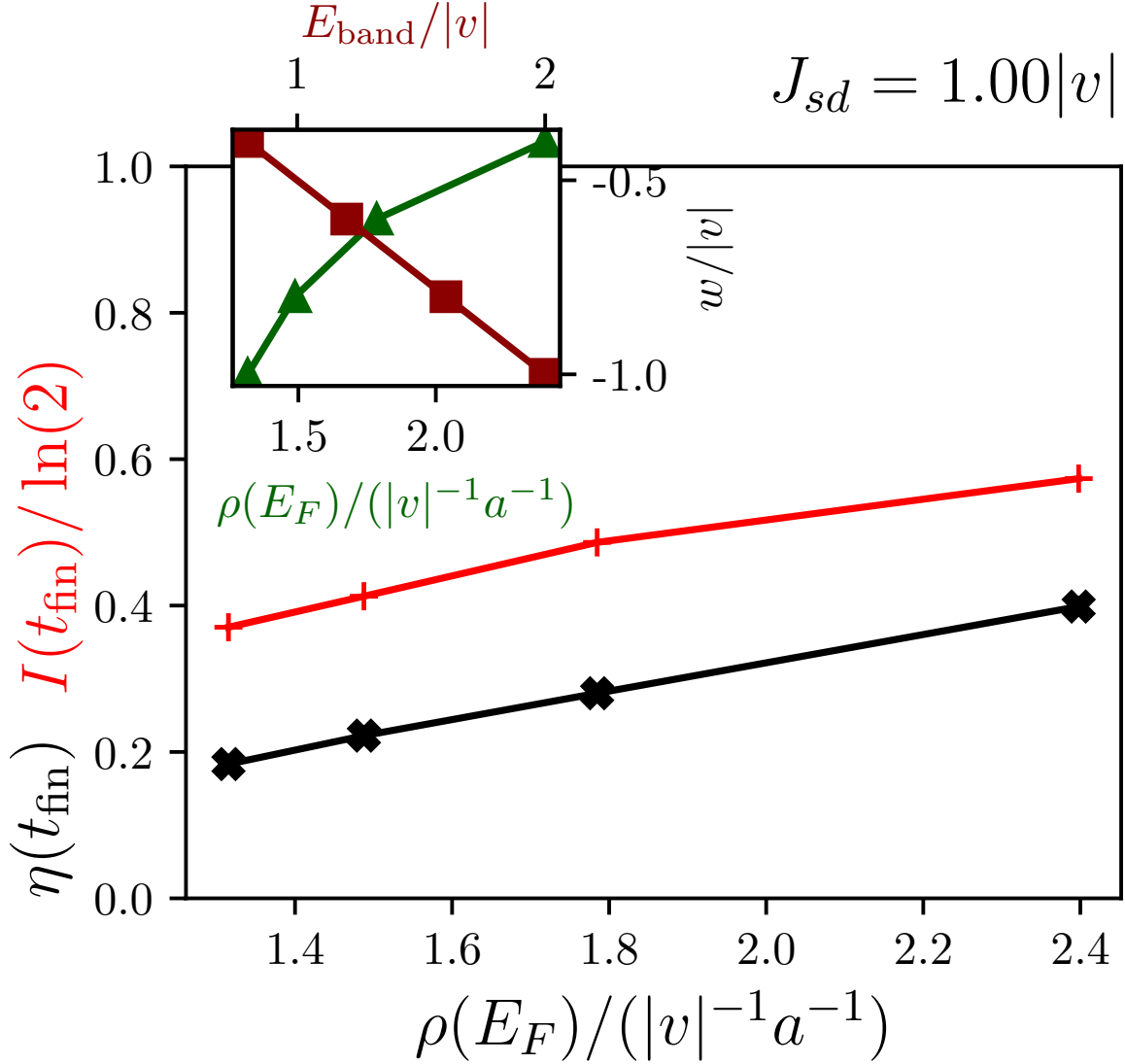


Figure 6: Quantum spin valve efficiency η [Eq. (5)] at the end of our simulations as a function of $\rho(E_F)$. Entanglement retained by the $|S\rangle$ MSQs at the end of our simulations, quantified by the mutual information I [Eq. (8)]. Both η and I correspond to a better quantum spin valve. Inset: the Rice-Mele hopping w dictates one-to-one the bandwidth E_{band} and the density of states at the Fermi energy $\rho(E_F)$.

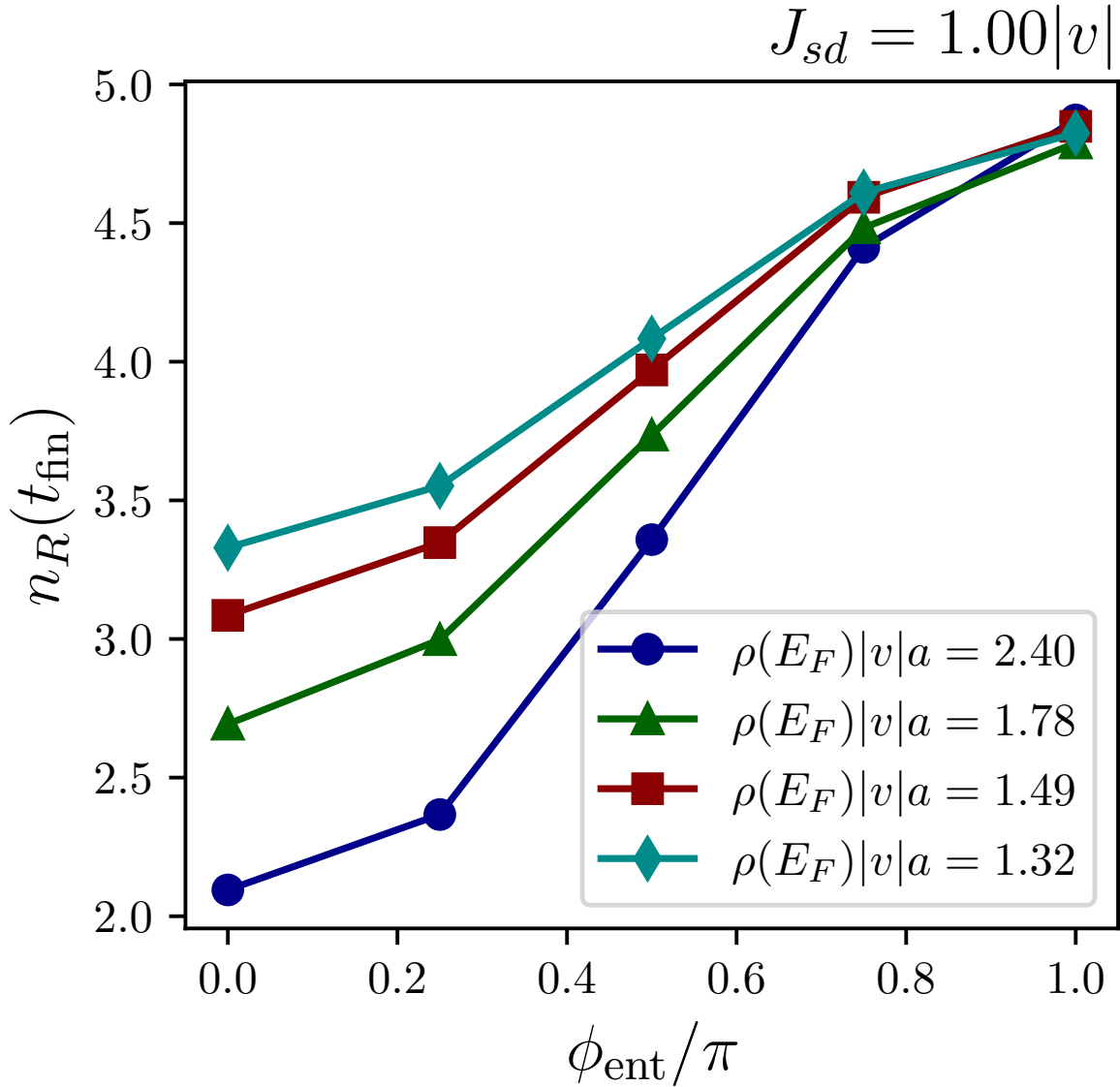


Figure 7: Electron accumulation n_R as we ‘open’ the spin valve by sweeping the phase ϕ_{ent} of the entangled state (1) from $\phi_{\text{ent}} = 0$ to $\phi_{\text{ent}} = \pi$. Notice how $\rho(E_F)$ dictates the disparity between the closed and open valve.

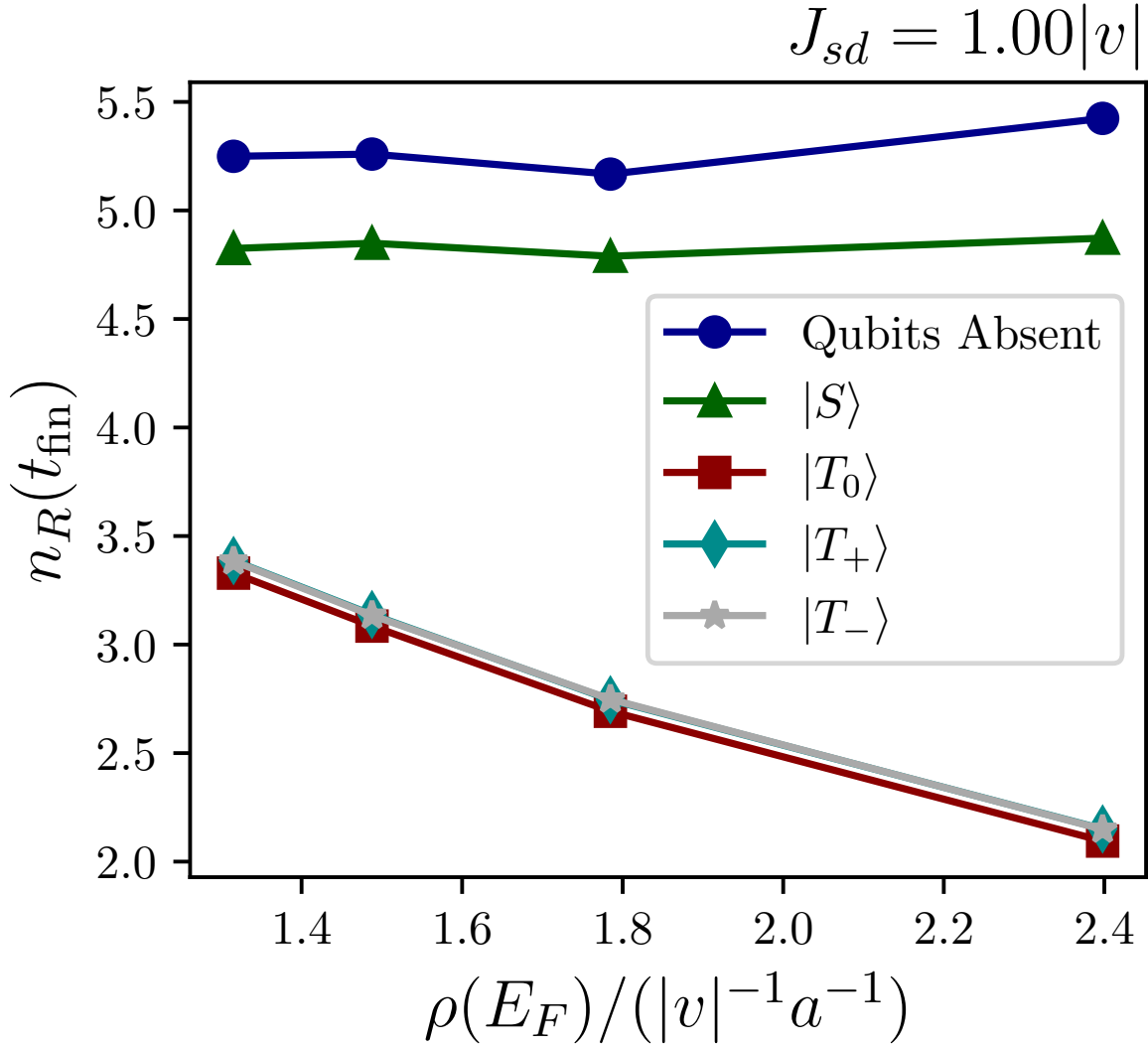


Figure 8: Electron accumulation n_R for $|S\rangle$ vs. all triplet states as a function of density of states at the Fermi energy $\rho(E_F)$. Enhancing $\rho(E_F)$ suppresses the conductance for all triplet states in tandem, making the $|S\rangle$ behavior stand out more clearly.

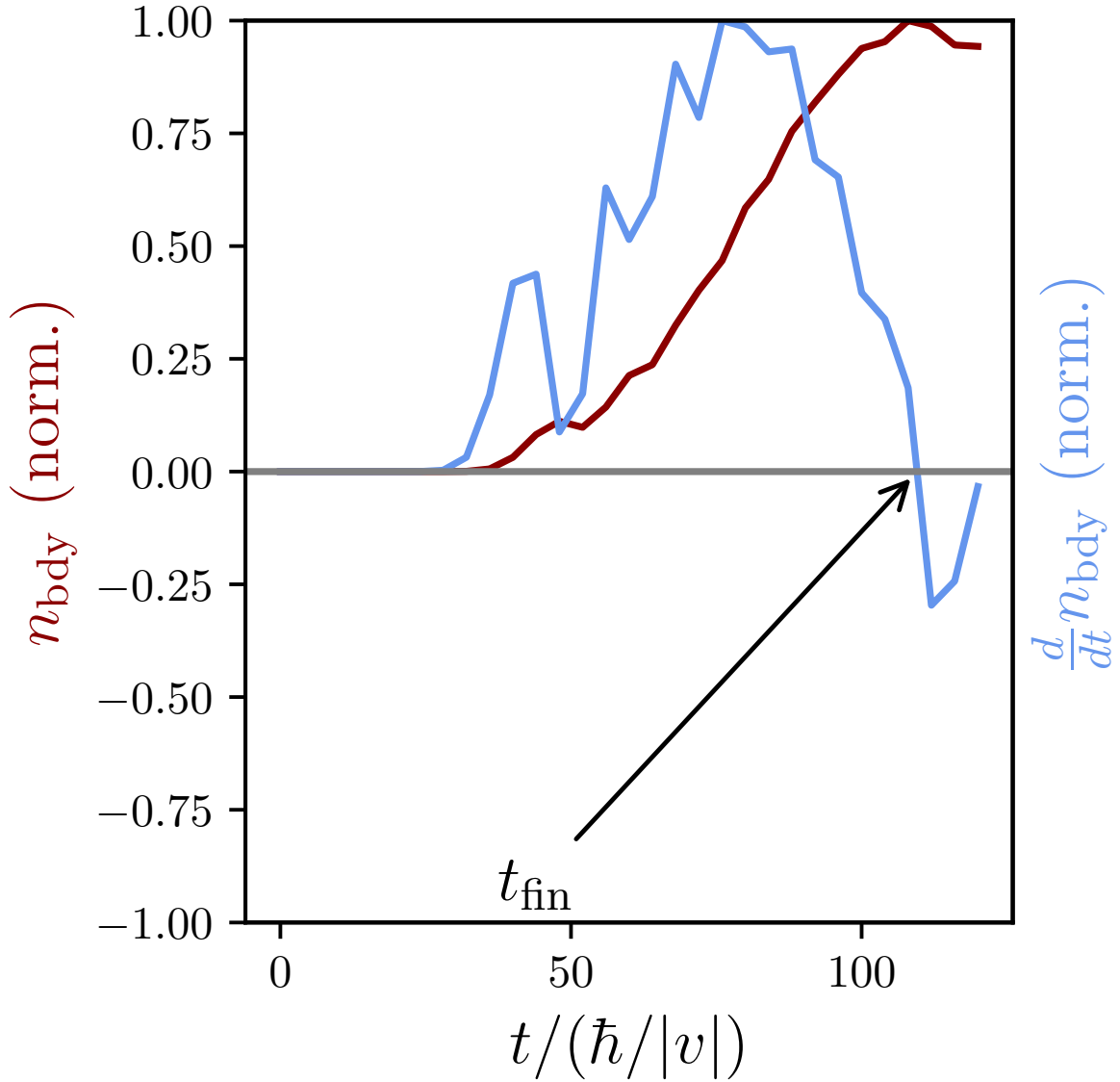


Figure 9: Onset of finite-size effects as the unphysical leftward reflection causes the occupation of the right boundary unit cell n_{bdy} to plateau and its derivative $\frac{d}{dt}n_{\text{bdy}}$ to change sign. Curves show $w = -0.40$, $N_e = 10$ simulation for qubits absent.

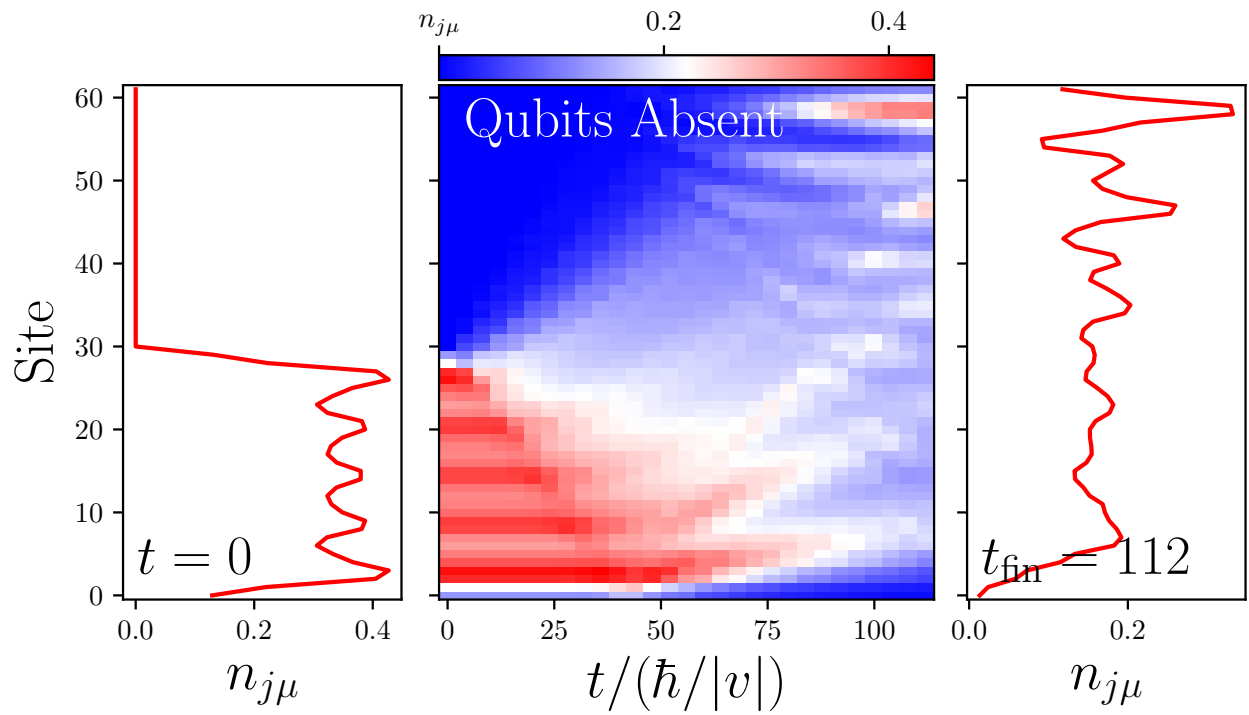


Figure 10: (left) site occupation $n_{j\mu}$ preceding quantum quench, (middle) full time and space dynamics of $n_{j\mu}$ following quantum quench, and (right) $n_{j\mu}$ at the end of the simulation. Throughout, Hamiltonian parameters are $w = -0.40$ and $N_e = 10$, geometric parameters are $N_L = N_R = 15$, $N_{\text{total}} = 31$ and td-DMRG parameters are $\chi_b = 250$, $dt = 0.1$.